Title

Distinct roles of nonmuscle myosin II isoforms for establishing tension and elasticity during cell morphodynamics

Authors

Kai Weißenbruch[1,2*], Justin Grewe[3,4*], Kathrin Stricker[1], Laurent Baulesch[1], Ulrich S. Schwarz[3,4+] and Martin Bastmeyer[1,2+]

[1] Zoological Institute, Karlsruhe Institute of Technology (KIT), 76128 Karlsruhe, Germany
[2] Institute of Functional Interfaces (IFG), Karlsruhe Institute of Technology (KIT), 76128 Karlsruhe, Germany
[3] Institute for Theoretical Physics, University of Heidelberg, Philosophenweg 19, 69120 Heidelberg, Germany
[4] BioQuant-Center for Quantitative Biology, University of Heidelberg, Im Neuenheimer Feld 267, 69120 Heidelberg, Germany

[+] To whom correspondence should be sent: schwarz@thphys.uni-heidelberg.de, bastmeyer@kit.edu.

* These authors contributed equally.

Abstract

Nonmuscle myosin II (NM II) is an integral part of essential cellular processes, including adhesion and migration. Mammalian cells express up to three isoforms termed NM IIA, B, and C. We used U2OS cells to create CRISPR/Cas9-based knockouts of all three isoforms and analyzed the phenotypes on homogeneous and micropatterned substrates. We find that NM IIA is essential to build up cellular tension during initial stages of force generation, while NM IIB is necessary to elastically stabilize NM IIA-generated tension. The knockout of NM IIC has no detectable effects. A scale-bridging mathematical model explains our observations by relating actin fiber stability to the molecular rates of the myosin crossbridge cycle. We also find that NM IIA initiates and guides co-assembly of NM IIB into heterotypic minifilaments. We finally use mathematical modeling to explain the different exchange dynamics of NM IIA and B in minifilaments, as measured in FRAP experiments.

Introduction

The morphodynamics of nonmuscle cells are strongly determined by the contractile actomyosin cytoskeleton, consisting of actin filaments and motor proteins of the nonmuscle myosin II (NM II) class (Chen et al., 2010; Gumbiner, 1996; Ingber, 2003; Vicente-Manzanares et al., 2009). The NM II holoenzyme is a hexamer consisting of two heavy chains (NMHC II) that form a homodimer, and four light chains: two regulatory light chains (RLCs) and two essential light chains (ELCs). Phosphorylation of the RLCs mediates the transition from the assembly-incompetent 10S to the assembly-competent 6S conformation of the NM II hexamer (Billington et al., 2013). Once activated, individual NM II hexamers assemble into bipolar filaments of up to 30 hexamers with a typical size of 300 nm, termed myosin minifilaments. These minifilaments can generate tension between antiparallel actin filaments due to their ATP-dependent motor activity. NM II generated forces are then transmitted throughout the cell by subcellular structures such as the actomyosin cortex and stress fibers (SFs). Adherent cells are anchored to the extracellular matrix (ECM) at integrin-based focal adhesions (FAs) where high forces can be measured with traction force microscopy (Balaban et al., 2001; Oakes et al., 2017).

Regulation of the actomyosin machinery enables cells to remodel their shape during motion-dependent processes like cell spreading, cell division, or cell migration (Heissler and Manstein, 2013; Svitkina, 2018; Vicente-Manzanares et al., 2009). In general, actomyosin contractility has to be continuously adapted to provide both, short-term dynamic flexibility and long-lasting stability (Ingber, 2003; Mandriota et al., 2019; Matthews et al., 2006). To precisely tune the contractile output, mammalian cells contain up to three different types of myosin II hexamers, which possess different structural and biochemical features. All hexamer-isoforms, which are commonly termed NM IIA, NM IIB and NM IIC, contain the same set of LCs but vary with respect to their heavy chains, which are encoded by three different genes. While the cell type-dependent expression, structure, and function of NM IIC is still not clear, the loss of NM IIA and NM IIB causes severe phenotypes in the corresponding KO-mice (Conti et al., 2004; Ma et al., 2010; Takeda et al., 2003; Tullio et al., 1997; Tullio et al., 2001; Uren et al., 2000). In addition, NM IIA and NM IIB are well characterized with respect to their structural and biochemical differences (Barua et al., 2014; Beach et al., 2017; Betapudi et al., 2006; Billington et al., 2013; Sandquist and Means, 2008; Sandquist et al., 2006; Shutova et al., 2012; Shutova et al., 2017; Vicente-Manzanares et al., 2007). NM IIA propels actin filaments 3.5× faster than NM IIB and generates fast contractions (Kovacs et al., 2003; Wang et al., 2000). NM IIB on the other hand can bear more load due to its higher duty ratio (Pato et al., 1996; Wang et al., 2003). Recent cell culture studies furthermore revealed that NM IIA and NM IIB hexamers co-assemble into heterotypic minifilaments, with a gradient from NM IIA to NM IIB content from the front to the rear of the cell (Beach et al., 2014; Shutova et al., 2014). However, it is still not clear how the interplay between the different NM II isoforms determines cellular morphodynamics. Here we address this question with a quantitative approach that combines cell experiments with mathematical modelling. To investigate the exact functions of the NM II isoforms during cellular shape determination, we used CRISPR/Cas9 technology to generate isoform-specific NM II-KO cells from the U2OS cell line, which is a model system for the investigation of SFs (Hotulainen and Lappalainen, 2006; Jiu et al., 2017; Lee et al., 2018; Tojkander et al., 2015; Tojkander et al., 2011).

For a quantitative analysis of cell shape, we used adhesive micropatterns (Lehnert et al., 2004; Ruprecht et al., 2017; Thery et al., 2006). Earlier we have investigated the cellular morphology of fibroblasts on dot-shaped micropatterns, where contractile cell types form a contour

consisting of a series of concave, inward bent actin arcs (Bischofs et al., 2008; Brand et al., 2017; Kassianidou et al., 2019; Labouesse et al., 2015; Tabdanov et al., 2018; Thery et al., 2006; Zand and Albrecht-Buehler, 1989). Invaginated actin arcs are circular and determined by the interplay of surface tension in the cell cortex and line tension in the cell contour, as described mathematically by a Laplace law (Bar-Ziv et al., 1999; Bischofs et al., 2008). A quantitative analysis revealed a correlation between the spanning distance of the actin arc and the arc radius, suggesting an elastic element in the line tension (tension-elasticity model, TEM). However, the underlying molecular reason for tensional and elastic elements remained unclear but now can be addressed with the newly generated NM II KO-cells.

We find that on homogeneously coated substrates, U2OS cells without NM IIA lack global tension and are unable to build up SFs or mature FAs, while the effect of a NM IIB knockout is less severe and only leads to cytoskeletal and adhesive structures that are less well defined. Quantitative cell shape analysis using cross-shaped adhesive micropatterns revealed that the patterns can partially rescue the phenotype of NM IIA-KO cells, suggesting that NM IIA is important for the initial generation of cytoskeletal tension in a homogeneous environment. For NM IIB-KO we find a breakdown of the relation between spanning distance and invaginated arc radius, suggesting that NM IIB is essential to elastically stabilize the NM IIA-generated tension. Thus, the adhesive micropatterns are essential to reveal a function that is not directly accessible on the homogenous substrates. In accordance with these findings, we show that NM IIA acts as the initiator of the actomyosin system by forming homotypic NM IIA pioneer minifilaments and triggering RLC-phosphorylation, which is almost completely missing in the NM IIA-KOs. NM IIC, although expressed in U2OS cells, seems to have hardly no role in morphodynamics.

To provide a mechanistic basis for these insights into the different cellular functions of the different NM II isoforms, we developed a mathematical model that bridges the molecular and cellular scales (dynamic tension-elasticity model, dTEM). The main molecular difference between the NM II isoforms are the different rates of their crossbridge cycles. We show that the faster crossbridge cycling of NM IIA not only leads to a more dynamic generation of tension (higher free velocity, smaller stall force, more dynamic and variable generation of invaginated shapes), it also leads to faster exchange dynamics in the NM II minifilaments, as confirmed by FRAP-experiments.

Together, our results demonstrate that NM IIA and NM IIB have clearly defined and distinct but complementary roles in establishing the morphology of single cells. While NM IIA is responsible for the dynamic generation of intracellular tension, most prominently at the front of polarizing cells, NM IIB is required to balance the generated forces by adding elastic stability to the actomyosin system, which for polarized cells is more important at the rear. These observations are in excellent agreement with the earlier finding that polarized cells form mixed minifilaments with a gradient of NM IIA to NM IIB from front to rear (Beach et al., 2014; Shutova et al., 2014) and now can be used to explain many tissue-related phenomena like e.g. collective cell migration (Scarpa and Mayor, 2016; Shellard and Mayor, 2019; Trepat and Sahai, 2018).

Results

NM II isoforms have a strong effect on stress fiber and focal adhesion formation on homogeneous substrates

To validate the impact of the different NM II isoforms on the cellular phenotype, we used U2OS cells. This cell line serves as a model for the investigation of SFs (Hotulainen and Lappalainen, 2006; Jiu et al., 2017; Lee et al., 2018; Tojkander et al., 2015; Tojkander et al., 2011) and expresses all three NM II isoforms (**Figure 1A and figure supplement 1D-F**). Since the NMHC II isoforms are encoded by three different genes, it is possible to generate isoform-specific NM II-KO cells. We used CRISPR/Cas9 to target the first coding exons of *MYH9*, *MYH10* and *MYH14,* encoding for NMHC IIA, NMHC IIB and NMHC IIC, respectively. For all NM II isoforms, stable cell lines lacking the protein of interest were subcloned. The loss of protein expression was confirmed by western blot analysis and immunofluorescence staining (**Fig. 1A and figure supplement 1A-C'**). In addition, DNA sequence analysis revealed that indels led to frameshifts and pre-mature stop codons in exon 2 of NMHC IIA and B (**Figure 1_figure supplement 1D-E**).

We first analyzed the NM II-KO phenotypes on homogeneously coated fibronectin (FN)-substrates and compared our data to previously reported results, where NM II isoforms were depleted via RNAi (Cai et al., 2006; Sandquist et al., 2006; Shutova et al., 2017; Thomas et al., 2015; Vicente-Manzanares et al., 2007) or genetic ablation (Bridgman et al., 2001; Conti et al., 2004; Even-Ram et al., 2007; Lo et al., 2004; Ma et al., 2010; Takeda et al., 2003; Tullio et al., 1997). We visualized SFs and FAs by staining for actin and the FA marker paxillin. Both elements are known to be affected upon interfering with actomyosin contractility (Even-Ram et al., 2007; Sandquist et al., 2006; Shutova et al., 2017; Vicente-Manzanares et al., 2007).

Polarized U2OS WT cells form numerous SFs of different subtypes, as previously described (Hotulainen and Lappalainen, 2006) (**Figure 1B**). Dorsal SF (dSF) localize along the leading edge and are connected to one FA on the distal end, transverse arcs (tA) align parallel to the leading edge in the lamellum and are not connected to FAs, ventral SF (vSF) localize in the cell center and are connected to FAs on both ends. Depletion of NM IIA leads to a markedly altered cellular phenotype with a branched morphology and several lamellipodia (**Figure 1C**). The cells are unable to build up an ordered SF-network with only few vSFs remaining. dSF or tAs were not observed. The remaining actin structures resemble a dense meshwork of fine, homogeneously distributed actin filaments. In a number of cells, long cell extensions remain, possibly reflecting remnants due to migration defects (Doyle et al., 2012; Even-Ram et al., 2007; Sandquist et al., 2006; Shih and Yamada, 2010). Mature, large FAs are absent in NM IIA-KO cells. Instead, numerous nascent adhesions with a point-like appearance localize along the cell edges, at the remaining vSF, and at the tips of the cell extensions. The effect of the NM IIB-KO is less severe and does not affect overall cell morphology (**Figure 1D**). All subtypes of SFs are present, but their distinct cellular localization was missing in many cells. In addition, numerous mature FAs were observed throughout the cell body but their localization appeared more diffuse. The depletion of NM IIC did not reveal any phenotypic differences compared to WT cells (**Figure 1E**).

We quantified the observed phenotypes by measuring cell area, FA size, and FA density (FA number / cell area). Only FAs ≥ 0.25 μm^2 were included in the measurements. Cell area does not significantly differ between WT and NM II-KO cell lines, indicating that cell spreading as such is not suppressed by the loss of any NM II isoform (**Figure 1_figure supplement 2C**).

Determination of the mean FA area revealed strongly reduced values for NM IIA-KO cells, a small reduction for NM IIB-KO cells, but no reduction for NM IIC-KO cells compared to WT cells (**Figure 1F**). Concerning FA density, we observed a strong reduction for NM IIA-KO cells, while NM IIB-KO and NM IIC-KO cells do not differ markedly from WT cells (**Figure 1G**). However, although the total number of FAs was not different, we found that larger FAs occurred less frequently in NM IIB-KO cells, while no difference was observed in NM IIC-KO cells (**Figure 1_figure supplement 2A&B**).

Taken together, our results using CRISPR/Cas9-generated U2OS-KO cell lines confirm earlier studies on cell lines derived from KO-mice or on RNAi-mediated knockdown cells (Cai et al., 2006; Even-Ram et al., 2007; Sandquist et al., 2006; Shutova et al., 2017). While the loss of NM IIA leads to drastic morphological changes, the loss of NM IIB only has mild effects. In addition, we could not observe any obvious morphological defects when depleting NM IIC.

Micropatterned substrates reveal distinct functions of NM IIA and NM IIB in cellular morphogenesis and force production

To gain a more complete understanding of the roles of the different NM II isoforms for cellular morphodynamics, we next used micropatterned substrates to normalize the phenotypes and quantitatively evaluated the corresponding results with the help of mathematical models. We produced cross-shaped FN-micropatterns via microcontact printing, which restrict FA formation to the pattern but still provide a sufficient adhesive area for the spreading of U2OS cells (see methods section for details). U2OS WT and all KO cell lines adapted their shape to the pattern and gained a striking phenotype with concave, inward bent actin arcs that line the cell contour as previously described for various cell types (**Figure 2**) (Bischofs et al., 2008; Brand et al., 2017; Kassianidou et al., 2019; Labouesse et al., 2015; Tabdanov et al., 2018; Thery et al., 2006). These arcs bridge passivated substrate areas and have a circular shape. NM II minifilaments localize along the circular actin arcs (**Figure 2_figure supplement 1**), suggesting that these peripheral arcs might be another type of contractile SF. From a geometrical point of view, the circularity results from two different NM II-based contributions to cell mechanics: tension in the cortex (surface tension σ) and tension in the actin arcs (line tension λ). Balancing these tensions can explain circular actin arcs with the radius $R = \lambda/\sigma$ (Laplace law). Typical order of magnitude values in this context are $R = 10\ \mu m$, $\lambda = 20$ nN and $\sigma = 2$ nN/μm. It was additionally shown that R depends on the spanning distance d between two adhesion sites, with larger d leading to larger R values (Bischofs et al., 2008). This dependence can be explained by assuming an elastic line tension $\lambda(d)$ (tension-elasticity model, TEM), suggesting that the mechanics of the peripheral SFs are not only determined by force generating NM II motors, but also by elastic crosslinking, e.g. by the actin crosslinker α-actinin.

To analyze differences in the NM II-KO cell lines, we measured arc radius R and spanning distance d and compared their correlation (see methods section for details). WT cells regularly form actin arcs along all cell edges (**Figure 2A**). Both, NM IIA and NM IIB co-localize with the actin arcs (**Figure 2_figure supplement 1A**). Quantitative evaluation showed a positive correlation ($r = 0.63 \pm 0.06$) of R with increasing d, as observed previously (Bischofs et al., 2008; Brand et al., 2017; Tabdanov et al., 2018). Surprisingly, NM IIA-KO cells formed circular arcs and also obeyed a clear $R(d)$-correlation ($r = 0.61 \pm 0.06$) (**Figure 2B**), despite the fact that their phenotype was strongly affected on homogeneously coated FN-substrates. This shows that the structured environment can partially rescue the phenotype. In detail, however, we noticed marked differences compared to WT cells. Although actin arcs along the cell edges

are still visible, they do not form as regular as in WT cells. The cell body often covers smaller passivated substrate areas but rather spreads along the crossbars, leading to smaller arcs. Only few NM IIB minifilaments co-localize along the actin arcs of NM IIA-KO cells and the pRLC staining was almost completely absent, suggesting that the absolute magnitudes of the contractile forces are low in these cells (**Figure 2_figure supplement 1B**). Most surprisingly, we found that the *R*(*d*) correlation was strongly reduced (r = 0.33 ± 0.09) in the NM IIB-KO cells (**Figure 2C**). Close inspection of the data suggest that this loss is caused by the presence of almost straight arcs that develop independent of the spanning distance *d*. Along these arcs, staining for NM IIA minifilaments and pRLC was comparable to WT cells (**Figure 2_figure supplement 1C**). In agreement with our results for homogeneously coated substrates, NM IIC-KO cells did not reveal any differences concerning their morphology and the *R*(*d*) correlation was comparable to WT cells (r = 0.63 ± 0.06) (**Figure 2D**). In summary, our experimental observations on the cross-shaped micropatterns reveal opposing effects for NM IIA and NM IIB in cell shape determination. NM IIA-KO cells form actin arcs with small arc radii that are correlated to the spanning distance, while NM IIB-KO cells form actin arcs with large arc radii that are not correlated to the spanning distance.

NM IIA and NM IIB contribute to dynamic generation of tension and elastic stability, respectively

To better understand these experimental results, we used mathematical models to connect our experimental findings to the molecular differences in the crossbridge cycle with NM IIA generating faster contractions (Kovacs et al., 2003; Wang et al., 2000) and NM IIB bearing more load (Pato et al., 1996; Wang et al., 2003). In contrast to our earlier work, where we developed a static tension-elasticity model (TEM), we now require a dynamical tension-elasticity model (dTEM), connecting the stationary cell shapes to the dynamic crossbridge cycling. We first note that due to geometrical constraints, the circular arcs on our cross-shaped micropattern can have central angles of only up to 90° as shown in **Figure 3A**, which defines a minimal radius $R_{min} = d/\sqrt{2}$ possible for a given spanning distance *d*. We next consider the SF as a dynamic contractile structure that sustains a continuous transport of cytoskeletal material from the FA towards the center of the SF (**Figure 3B**). This flow can be observed experimentally in vSFs for cells on homogeneously coated substrates and in peripheral arcs for cells on cross-shaped micropatterns (**Figure 3_figure supplement 1 and Figure 3_movies 1&2**) and, like retrograde flow, is believed to be driven by both actin polymerization in the FAs and myosin-dependent contractile forces (Endlich et al., 2007; Hu et al., 2017; Oakes et al., 2017; Russell et al., 2011; Tojkander et al., 2015). Therefore, it should also depend on the isoform specific motor properties that result from the differences in the crossbridge cycles. Like in muscle cells, mature SFs are organized with sarcomeric arrangements of the myosin motors (Dasbiswas et al., 2018; Hu et al., 2017). Accordingly, the number of serially arranged myosin motors increases linearly with SF length, and SF contraction speed should also increase with length. The stall force F_s, however, should not depend on the SF length because in this one-dimensional serial arrangement of motors, each motor feels the same force. A linear scaling between contraction speed and length, as well as the length-independence of the stall force has indeed been observed experimentally in reconstituted SFs (Thoresen et al., 2013). Using an established model for the crossbridge cycle (**Figure 3C**) and the known differences between the powerstroke rates of NM IIA and NM IIB, we can calculate the stall force F_s for homotypic and heterotypic minifilaments (Grewe and Schwarz, 2020a; Grewe and Schwarz, 2020b). We find that with increasing NM IIB content, the stall force increases and the free velocity decreases (**Supplemental text and supplement**

figure S1). For the polymerization at FAs, we assume that its rate increases with force, as has been shown in vitro for mDia1, the main actin polymerization factor in FAs (Jegou et al., 2013). Combining these molecular elements with the geometrical considerations of the TEM (details are given in the supplemental text), we arrive at a surprisingly simple form for the *R*(*d*) relation:

$$R(d) = \frac{d}{d_m + d} R_{max} \quad (1)$$

The maximal radius $R_{max} = F_s/\sigma$ is given by the ratio of stall force F_s and surface tension σ. It can be understood as the arc radius that would be observed if there was no reduction of the tension by the inflow from the FAs and corresponds to the static TEM with the stall force providing the line tension. The spanning distance at half maximal radius results from the relative steepness of the force-velocity relations of SFs and FAs (expressed as friction coefficients, compare supplemental text) and defines whether the force is determined by the contraction speed of the fiber or the stall force of the motors. If the spanning distance is small against d_m, the observed radius scales linearly with the length of the SF, while at spanning distances large against d_m, the radius becomes independent of length and is primarily governed by stall force and surface tension.

Fitting eq. (1) to the experimental data shown in Figures 2A-D yield the parameters R_{max} and d_m for each cell line (solid lines, dashed lines show the minimum radius resulting for a central angle of 90°). The mean fit values and standard deviations for the invaginated arcs are calculated from bootstraps and are listed in table 1. Note that the fit for NM IIB-KO is not entirely meaningful, because a clear correlation is not present in this case. By rescaling the experimental values using the fit parameters, the data points roughly follow a master curve (Figure 3D). This illustrates that the data for WT, NM IIA-KO and NM IIC-KO cells lie in the linear regime, while the data for NM IIB-KO lie in the plateau regime. At the same time, the independence of spanning distance *d* also reflects the breakdown of the correlation, suggesting that NM IIB is relevant to elastically stabilize the arcs. For NM IIA, we conclude that its main function is to dynamically generate tension, because its KO leads to smaller arcs due to missing contractility. Yet, in this case σ and λ are balanced and lead to clear correlations since NM IIB still serves as an elastic stabilizer.

To further separate the different phenotypes, we plot our data in the two-dimensional parameter space of $(d_m/R_{max}, d/R_{max})$ (Figure 3E). The shaded region denotes allowed values due to the central angle being smaller than 90°. Strikingly, the ratio d_m/R_{max}, which scales linearly with the ratio of SF friction and motor stall force, increases with the relative amount of NM IIB in the SF, from NM IIB-KO, over WT and NM IIC-KO cells to NM IIA-KO cells. This agrees with our theoretical finding that the ratio of friction and stall force is proportional to the average dwell time of NM II on actin during the crossbridge cycle (Grewe and Schwarz, 2020a; Grewe and Schwarz, 2020b), which is much larger for NM IIB compared to NM IIA. Together these results suggest that the larger dwell time of NM IIB translates directly into larger radii and stronger arcs.

Our results for the NM IIA-KO cells in Figure 3E are closest to the edge of the region with the theoretically permissible arcs, which suggests that in general some arcs cannot form because of geometrical constraints. Our model allows us to further investigate this aspect. Figures 3F-H show that the distribution of the difference of observed radius to the minimum radius, normalized to the minimum radius approximately follows a Gaussian distribution that is, however, cut off at zero difference. Assuming that the missing part of the distribution

corresponds to the fraction of arcs that have not formed, we find that there should be approximately 10%, 18% and 7% non-formed arcs for WT, NM IIA-KO and NM IIB-KO cells, respectively. This again suggests that NM IIA is the most important isoform for the formation of arcs, while NM IIB is more important for stabilization.

To further investigate the identified roles of NM IIA versus B, we reconstituted NM IIA protein function in NM IIA-KO cells using different NMHC IIA mutants (Breckenridge et al., 2009; Dulyaninova et al., 2007; Dulyaninova et al., 2005; Rai et al., 2017) (**Figure 3_figure supplement 2**). We find that prolonged NM IIA dwell times in the minifilaments reduced the *R*(*d*) correlation, also in the presence of endogenous NM IIB (**Figure 3_figure supplement 2&3**). Mutants, in which the disassembly of the NM IIA hexamers was blocked, showed a weaker *R*(*d*) correlation (**Figure 3_figure supplement 2D&E**), while the WT or a constitutively active NMHC IIA construct did not affect the *R*(*d*) correlation (**Figure 3_figure supplement 2A&C**). This demonstrates that spatially and temporally balanced ratios of active NM IIA and NM IIB hexamers in heterotypic minifilaments are mandatory to adjust the contractile output in SFs and the relation between tension and elasticity. Therefore, the specific biochemical features of the isoforms and not their overall expression are important for the generation of tension and elastic stability, respectively.

NM IIA induces global actomyosin contractility and amplifies NM IIB activity

Having characterized the distinct roles of the isoforms NM IIA and B, we next asked how they cooperate on the cellular level. NM IIA or NM IIB minifilaments were visualized by immunostaining phosphorylated RLCs (pRLC) together with NMHC IIA or NMHC IIB in either WT, NM IIA-KO or NM IIB-KO cells (**Figure 4A**). Whereas pRLC stainings label the head regions of all active NM II minifilaments, NMHC IIA or NMHC IIB signals are isoform-specific. In polarized WT cells with a clearly defined single lamellipodium, NMHC IIA and pRLC signals co-localize throughout the cell body whereas NMHC IIB signals are enriched in the cell center (**Figure 4B&C**), confirming previous findings (Beach et al., 2014; Kolega, 1998; Shutova et al., 2012; Shutova et al., 2014). Surprisingly, the pRLC staining was almost completely absent in NM IIA-KO cells, indicating that the activation of NM II hexamers was very low (**Figure 4B&D**). In line with this finding, the occurrence of NM IIB minifilaments was strongly reduced and the remaining minifilaments localized along the few vSFs. In contrast, pRLC signal intensity and NM IIA minifilament frequency were unaffected in NM IIB-KO cells (**Figure 4C&D**).

RLC phosphorylation as well as NM IIB minifilament frequency could be restored in NM IIA-KO cells by expressing GFP-tagged NMHC IIA. In addition, we observed a linear correlation between the pRLC signal intensity and NM IIA expression ratio (**Figure 4_figure supplement 1A&B**). A constitutively active NMHC IIA (GFP-NM IIA-ΔIQ2), where the binding site for the RLC was removed (Breckenridge et al., 2009), did not restore pRLC intensity but the frequency of NM IIB minifilaments (**Figure 4_figure supplement 1A&C**). In contrast, overexpression of GFP-tagged NMHC IIB did not restore the pRLC level or the frequency of NM IIB minifilaments in NM IIA-KO cells (**Figure 4_figure supplement 1 D&E**).

Since the overall activation of NM II hexamers and frequency of NM IIB minifilaments is strongly affected by the loss of NM IIA, we also tested whether NM IIA acts upstream of NM IIB during the formation of heterotypic minifilaments, as previously suggested (Shutova et al., 2017; Shutova et al., 2014). Indeed, we found that all heterotypic minifilaments arise from homotypic NM IIA minifilaments, in which NM IIB hexamers co-assemble over time (**Figure 4_figure supplement 2**). While the ratio of NM IIA and NM IIB changed with regard to the

centripetal actin flow in polarized cells, it remained constant in non-polarized cells (**Figure 4_figure supplement 2F**). In all cases, we rarely observed homotypic NM IIB minifilaments, suggesting that heterotypic minifilaments represent the majority of contractile units in single cells. Taken together, our results indicate that minifilaments are initially formed by NM IIA, while NM IIB hexamers are incorporated later.

NM IIA and NM IIB hexamers bear different exchange dynamics in minifilaments

Our mathematical model suggests that the crossbridge cycle rates of the different NM II isoforms directly translate into different arc stability. In order to analyze in more detail the intermediate step of minifilament assembly, we next performed FRAP (fluorescence recovery after photobleaching) studies on both paralogs (**Figure 5A&B and Figure 5_movies 1&2**). For that purpose, we again utilized our KO cell lines to reconstitute the respective GFP-tagged isoform, thus avoiding the interference with endogenous NM IIA or NM IIB. We measured the recovery rates of NM IIA or NM IIB in the absence or presence of photostable Para-Aminoblebbistatin (**Figure 5C**) (Varkuti et al., 2016). When comparing the recovery times (**Figure 5D**) and mobile fractions (**Figure 5E**), we find that the exchange rate of NM IIA is much faster compared to NM IIB. While NM IIA shows a mobile fraction of 63 ± 29% with an exchange timescale of 69 ± 53 s, NM IIB possesses a lower mobile fraction of 47 ± 28% with a higher exchange timescale of 230 ± 140 s. These results are in line with previously published results from other groups that measured FRAP dynamics by overexpressing NM IIA or NM IIB in different cell lines (Sandquist and Means, 2008; Shutova et al., 2017; Vicente-Manzanares et al., 2008; Vicente-Manzanares et al., 2007). In accordance with our previous findings, this shows that NM IIA is predestined to dynamically build up tension, since it disassembles faster from the minifilament and thereby enables a rapid rearrangement of the contractions where necessary. NM IIB on the other hand stays longer bound in the minifilaments, thereby stabilizing the NM IIA-generated tension.

In the presence of the photostable Para-Aminoblebbistatin, we find that NM IIA and NM IIB possess the same recovery dynamics for both, mobile fraction and recovery time (**Figure 5D&E**). For NM IIA in the presence of para-aminoblebbistatin, we find a mobile fraction of 55 ± 34% with recovery timescales of 52 ± 30 s, while for NM IIB, a mobile fraction of 64 ± 33% with recovery timescales of 62 ± 44 s were observed. Since recovery timescale and mobile fraction are not statistically independent variables as they arise from the same fit (and are correlated), we compared the joint distribution of both observables by a two-dimensional version of the Kolmogorov-Smirnoff test, the Peacock test (Fasano and Franceschini, 1986; Peacock, 1983). Comparing our different conditions revealed significant differences only between NM IIB in the absence of para-aminoblebbistatin and all other experimental situation (**Figure 5D&E**). Blebbistatin and presumably also its derivatives are known to target the tension generation of myosin II (Kovacs et al., 2004). The force-generating step of the crossbridge cycle, which is linked to phosphate release, is slowed down. As the differences in the FRAP experiments between NM IIA and NM IIB, which probe the assembly dynamics of myosin minifilaments, are leveled in the presence of para-aminoblebbistatin, we interpret our result as evidence for an interdependence of the assembly of NM II minifilaments and their mechanochemical crossbridge cycle.

Aiming for a mechanistic understanding of this effect, we next used a NM II minifilament assembly model that couples the crossbridge cycle and the dynamic self-assembly to simulate the FRAP data (Grewe and Schwarz, 2020a; Grewe and Schwarz, 2020b). In brief, to model the association and dissociation dynamics we start with a consensus architecture of the ~30

NM II hexamers that form a minifilament. Minifilaments are known to result from a very stable anti-parallel stagger that is complemented at the sides by parallel staggers (**Figure 6A**). In three dimensions, three such arrangements form a cylindrical structure that can be represented by an appropriate graph (**Figure 6B**). The presence or absence of fluorescent species can be simulated by using appropriate labels. The neighborhood relations of each NM II give rise to specific binding energies determined mainly by the electrostatic interactions of charged regions on the coiled-coils of the NM II hexamers (Kaufmann and Schwarz, 2020). All NM II hexamers in the assembly in principle can interact with actin via the crossbridge cycle shown schematically in **Figure 3C**, thereby producing force. The presence of blebbistatin is reflected in a strong reduction of the rate at which the powerstroke occurs (rate k_{12} in **Figure 3C**). In our computer simulations, we assume that NM II hexamers cannot detach from the minifilament while they are part of the assembly (more details on the model and model parameters in the **supplemental text**).

We started by simulating NM IIA minifilaments in the absence of blebbistatin which we used to calibrate the association rate to the experimental data. We obtained reasonable agreement with an association rate of $k_{on} = 5$ s^{-1}, which we held constant in the following simulations. The simulated FRAP data is shown in **Figure 6C**. Simulating NM IIA in the presence of blebbistatin showed little change, consistent with the experiment. Simulating NM IIB with its slower detachment from the post powerstroke state showed slower recovery dynamics that became comparable with the results for NM IIA. The timescales and mobile fractions are summarized in **Figures 6D and E**. We note that the NM IIB recovery times do not quantitatively match the experiments very well. Using an even slower detachment rate from the post powerstroke state gives better results, suggesting that the NM IIB post-powerstroke detachment may depend even more strongly on force than assumed in our current model. Overall, however, our model is able to capture the effects that blebbistatin has on the FRAP dynamics. This confirms that the known differences in the crossbridge cycle of the two isoforms NM IIA and B can explain not only the differences in shape on the cell level, but also the differences in exchange dynamics on the subcellular level.

Discussion

Here we have systematically and quantitatively analyzed the roles of the three different NM II isoforms for cellular morphodynamics using a combined experimental and theoretical approach. Due to CRISPR/Cas9 technology, we were able to analyze all three NM II isoforms simultaneously from the same cellular background. By using geometrically defined micropatterns in combination with quantitative image processing and mathematic modeling, we were able to provide a detailed picture about the complementary functions of NM IIA and NM IIB: generation of dynamic tension by NM IIA and elastic stabilization by NM IIB. In this way, the cytoskeletal scaffold provides both, short-term dynamic flexibility and long-lasting stability, allowing cells to dynamically adapt their shapes to varying extracellular geometries and topographies. While NM IIA and B led to distinct phenotypes, NM IIC plays a much less prominent role in this context, at least when NM IIA and B are expressed at the same time.

Validating our U2OS NM II-KO cells on homogeneously coated substrates confirmed previous reports about NM IIA and NM IIB (Even-Ram et al., 2007; Sandquist et al., 2006; Shutova et al., 2017; Vicente-Manzanares et al., 2011; Vicente-Manzanares et al., 2007). Without NM IIA, cells possess a branched morphology and lack SF and mature FA. The NM IIB-KO only leads to a less clear distinction between different types of SF and smaller FA. Although we noticed some differences in NM IIB-KO cells, distinctive phenotypic features were difficult to evaluate due to variations in the cell morphology and actomyosin architecture on homogeneously-coated coverslips. Normalizing the cellular phenotypes on micropatterned substrates allowed precise quantification of morphological differences in NM IIA-KO and NM IIB-KO cells. Different NM II-KO's lead to marked changes in the relations between the spanning distance and the radius of invaginated actin arcs. NM IIA-KO cells form small arcs and fail to surpass larger passivated substrate areas. Instead, actin is polymerized along the cross-shaped pattern. However, the arc radii are still related to its spanning distance. In contrast, NM IIB-KO cells form large actin arcs, which are rather poorly correlated with the spanning distance.

No obvious phenotypic change or disturbance in the $R(d)$ correlation was observed when depleting NM IIC. Thus, our results indicate that NM IIC is less important for the global generation of traction forces. Since this is the first time that NM IIC was depleted in U2OS cells, we can only speculate about its function. Structural *in vitro* analysis revealed that NM IIC minifilaments are smaller compared to their paralog counterparts (Billington et al., 2013). This could suggest that NM IIC has a role as a scaffolding protein during the formation of higher ordered NM IIA minifilaments stacks, comparable to the role of myosin-18B (Jiu et al., 2019). In line with this, Beach and colleagues reported that NM IIA and NM IIC co-localize throughout the whole cell in U2OS cells (Beach et al., 2014). Concerning other cell types, accumulations of NM IIC along the apical junctional-line have been reported (Ebrahim et al., 2013) and a role for NM IIC during cytokinesis in A549 cells was suggested (Jana et al., 2006).

By connecting the observations concerning NM IIA and B to our dynamic tension-elasticity model (dTEM), we can explain the observed phenotypic differences by differences in the molecular crossbridge cycles. NM IIA-KO cells still possess NM IIB-derived elastic stability but lack dynamic tension leading to low intracellular forces. The phenotype of NM IIA-KO cells was, however, partially restored on the micropattern, suggesting that the main function of NM IIA is guidance of the actomyosin system in the absence of external guidance cues. Since the generation of contractile actomyosin bundles is a mechanosensitive process (Tojkander et al., 2015), a polarized actomyosin cytoskeleton is missing in NM IIA-KO cells. Without fast NM IIA motors, NM IIB is too slow to rearrange the contractile forces in accordance with the

fast turnover of actin filaments. Consequently, the only remaining SF resemble vSF, because their turnover is lowest (Kumar et al., 2006; Lee et al., 2018). As FA are also known to mature in a force-dependent manner (del Rio et al., 2009; Schiller et al., 2013; Vicente-Manzanares et al., 2007), only nascent adhesions remain in the cell periphery and at vSF. NM IIB-KO cells in contrast still possess NM IIA minifilaments, which induce the actomyosin system and generate sufficient but unbalanced intracellular forces. In polarized WT cells, NM IIB is enriched in the central part of the cell and stabilizes vSFs, while higher dynamics arise in NM IIA enriched tAs and indirectly connected dSF (Shutova et al., 2017; Vicente-Manzanares et al., 2008). Since the stabilizing function is missing in NM IIB-KO cells, the fast motor dynamics of NM IIA lead to a high degree of tension, independent of the SF subtype. Although the fast and dynamic motor activity of NM IIA is sufficient to induce the mechanosensitive assembly of all SF subtypes, their distinct localization is disturbed. Likewise, loss of NM IIB does not affect the formation of FAs, however, they do not grow to full size, since the actin templates, in particular the vSFs, are not sufficiently stabilized by the cross-linking properties of NM IIB.

This interpretation shows how the complementary biochemical features of NM IIA and NM IIB cooperate to build up and maintain a polarized actomyosin cytoskeleton in WT cells. While NM IIA is responsible for the dynamic generation of intracellular tension, most prominently at the cell front of polarized cells, NM IIB is required to balance the generated forces by adding elastic stability to the actomyosin system, which for polarized cells is more important at the rear. To achieve this highly ordered actomyosin structure, NM II minifilaments assemble in a precisely regulated temporal manner. The activation of the entire NM II population depends on the presence of NM IIA, again showing that this isoform is the key player to globally induce and guide the actomyosin system. While the loss of NM IIA almost completely abolished the pRLC signal and number of NM IIB minifilaments, depleting or overexpressing NM IIB did not affect the pRLC signal or number of NM IIA minifilaments. Taking into account that tension has to be generated before it can be stabilized, the initiation of the actomyosin system follows a logical order: NM IIA acts as the initiating building block by forming the pioneer minifilaments, in which NM IIB is progressively incorporated over time. This hypothesis is in line with the work of other groups, who showed that heterotypic minifilaments exist in living cells (Beach et al., 2014; Shutova et al., 2017; Shutova et al., 2014) and that NM IIA is able to dynamize and regulate the NM IIB distribution in the cell (Shutova et al., 2017). This scenario is further supported by a recent theoretical study on the relative stability of mixed filaments (Kaufmann and Schwarz, 2020).

We further strengthened these interpretations using FRAP measurements, which showed that the exchange dynamics of NM IIA are much higher than for NM IIB. We measured the recovery rates in reconstituted NM IIA- or NM IIB-transfected cells to avoid a possible interference due to endogenous protein levels and/or overexpression artefacts. The slow recycling of NM IIB suggests that polymerized NM IIB minifilaments stay bound to the actin cytoskeleton longer than NM IIA minifilaments and therefore are prone to maintain tension on a longer timescale. In contrast, the more dynamic NM IIA can quickly repopulate new formed protrusions and initiate new contraction sites via its fast and dynamic crossbridge cycle. Importantly, NM IIA not only initiates and determines the localization of the contraction, but also the amplitude. When the exchange rate of NM IIA is inhibited by preventing NMHC IIA phosphorylation, the $R(d)$ correlation was lost, suggesting that the specific intracellular force output is precisely tuned by the ratio and dwell time of individual NM IIA and NM IIB hexamers in the heterotypic minifilaments. However, these processes do not only depend on the properties of the motors

and their assemblies, but also on the structural organization of the actin cytoskeleton. In the future, our approach should be complemented by imaging and modelling of the actin cytoskeleton using super-resolution microscopy (Martinez et al., 2020; Qi et al., 2019; Shelden et al., 2016; Wassie et al., 2019). In a next step, our insights into the distinct cellular roles of the different NM II isoforms should be transferred to the tissue context, e.g. to explain collective migration effects in development, wound healing or cancer (Scarpa and Mayor, 2016; Shellard and Mayor, 2019; Sunyer et al., 2016; Trepat and Sahai, 2018).

Materials and Methods

Cell Culture: U2OS WT cells were obtained from the American Type Culture Collection (Manassas, USA). U2OS NM II-KO cell lines were generated as described in the following section. All cell lines were tested for mycoplasma infection with negative results. For routine cultivation, cells were passaged every 2-3 days and maintained in DMEM (Pan-Biotech #P04-03590) supplemented with 10% bovine growth serum (HyClone #SH3054.03) at 37°C under a humidified atmosphere containing 5% CO_2. For experiments, cells were plated on FN-coated coverslips or micropatterned substrates and allowed to spread for 3 h.

Generation and validation of NM II-KO cell lines: NM II-KO cell lines were generated by CRISPR/Cas9 according to the guidelines in (Ran et al., 2013). Briefly, U2OS WT cells were transfected with the single plasmid system from Feng Zhang's lab (Addgene #62988). Guide sequences for the respective protein of interest were determined using the online tool "CHOPCHOP" (https://chopchop.cbu.uib.no/). The sgRNAs were designed to target all known splice variants of NMHC IIB and NMHC IIC. All used guide sequences are depicted in 5′-to-3′ direction in Table 2. Oligos for gRNA construction were obtained from Eurofins genomics (Ebersberg, Germany) and cloned into pSPCas9(BB)-2A-Puro (PX459) V2.0. To select for transfected cells, 5 µg mL^{-1} puromycin was added 48 h post transfection to the culture medium and the cells were selected for another 48 h. Cell clones were screened for loss of protein expression by western blot and immunofluorescence.

Western blotting: A confluent monolayer of cells in a 6-well plate was scraped from the dish using 150 µl ice-cold lysis buffer (187 mM Tris/HCl, 6% SDS, 30% sucrose, 5% β-mercaptoethanol), heated at 95°C for 5 min and centrifuged at 13,000 rpm for 10 min. About 30 µl of the supernatant was loaded onto an 8% gel. The proteins were resolved by SDS-PAGE and transferred to a PVDF membrane by tank blotting at 150 mA for 2 h using the Miniprotean III System from Bio-Rad (Hercules, USA). The membrane was blocked for 1 h with 5% skim milk in PBS containing 0,05% Tween-20. The following antibody incubation steps were also carried out in the blocking solution. Primary antibodies were applied over night at 4°C and secondary antibodies for 2 h at room temperature. In between and after the antibody incubation steps, membranes were washed in PBS/Tween-20. Following primary antibodies were used: mouse monoclonal to α-Tubulin (Sigma-Aldrich #T5168), rabbit polyclonal to NMHC IIA (BioLegend, #909801), rabbit polyclonal to NMHC IIB (BioLegend, #909901), rabbit monoclonal to NMHC IIC (CST, #8189S). Secondary horseradish peroxidase-coupled anti-mouse or anti-rabbit antibodies were from Jackson Immunoresearch (#711-036-152 and #715-035-150). The membranes were developed with the SuperSignal™ West Pico PLUS chemiluminescent substrate (ThermoFisher Scientific #34579) according to manufacturer's instructions. Signal detection was carried out using an Amersham Imager 600 from GE Healthcare (Chicago, USA).

Sequence analysis: gDNA was isolated using the DNeasy Blood & Tissue Kit (Qiagen #60506) and the target region was amplified via PCR. Primers were designed using the Primer3 freeware tool (Untergasser et al., 2012) and purchased from Eurofins genomics (Ebersberg, Germany). All used primers are listed in table 2. PCR products were either cloned into the pCR II-Blunt-TOPO vector using the Zero Blunt® TOPO® PCR cloning kit (ThermoFisher Scientific #K2875J10) for subsequent sequencing or sequenced directly. Sequencing was carried out at LGC Genomics (Berlin, Germany) and the results were compared to WT sequences using the free available version of SnapGene Viewer (www.snapgene.com/snapgene-viewer).

Transfection and constructs: Transfection was carried out using Lipofectamine 2000 (ThermoFisher Scientific #11668027) according to manufacturer's instructions and the cells were cultivated for 48 h before the experiment. CMV-GFP-NMHC IIA (Addgene #11347) and CMV-GFP-NMHC IIB (Addgene #11348) were gifts from Robert Adelstein (Wei and Adelstein, 2000). NMHC IIA-mApple was a gift from Jordan Beach (Loyola University, Chicago, USA). pCMV-eGFP-NMHC IIA-ΔIQ2 (Addgene #35690), pCMV-eGFP-NMHC IIA-ΔNHT (Addgene #35689) and pEGFP-NMHC IIA-3xA (Addgene #101041) were gifts from Tom Egelhoff (Breckenridge et al., 2009; Rai et al., 2017). CMV-GFP-NMHC IIA-ΔACD was produced by digesting CMV-GFP-NMHC IIA with SacII and SalI, removing the final 808 bp of the CDS of NMHC IIA and thereby deleting the assembly-competence domain (ACD). pSPCas9(BB)-2A-Puro (PX459) V2.0 was a gift from Feng Zhang (Addgene #62988). Guide sequences for the generation of NMHC II depleted cells were introduced by digesting the plasmid with BbsI and subsequent ligation of the insert and vector (Ran et al., 2013).

Fabrication of micropatterned substrates: Micropatterned substrates were prepared using the microcontact printing technique (Mrksich and Whitesides, 1996). Briefly, a master structure was produced by direct laser writing (Anscombe, 2010) to serve as a negative mould for a silicon stamp. The pattern of the stamp resembles a sequence of crosses with different intersections, a bar width of 5 µm and edge length of 45-65 µm. The pattern was either transferred using gold-thiol chemistry (Mrksich et al., 1997) or direct microcontact printing (Fritz and Bastmeyer, 2013). When using gold-thiol chemistry, the stamp was inked with a 1.5 mM solution of octadecylmercaptan (Sigma Aldrich #O1858) in ethanol and pressed onto the gold-coated coverslip, forming a self-assembled monolayer at the protruding parts of the stamp. For the subsequent passivation of uncoated areas, 2.5 mM solution of hexa(ethylene glycol)-terminated alkanethiol (ProChimia Surfaces #TH-001-m11.n6) in ethanol was used. Micropatterned coverslips were functionalized with a solution of 10 µg mL-1 FN from human plasma (Sigma Aldrich #F1056) for 1 h at room temperature. For direct microcontact printing, stamps were incubated for 10 min with a solution of 10 µg ml^{-1} FN and pressed onto uncoated a coverslip. Passivation was carried out using a BSA-Solution of 10 mg ml^{-1} in PBS for backfilling of the coverslip at room temperature for 1 h.

Immunostaining: Samples were fixed for 10 min using 4% paraformaldehyde in PBS and cells were permeabilized by washing three times for 5 min with PBS containing 0.1% Triton X-100. Following primary antibodies were used: mouse monoclonal to FN (BD Biosciences, #610078), rabbit polyclonal to NMHC IIA (BioLegend, #909801), rabbit polyclonal to NMHC IIB (BioLegend, #909901), rabbit monoclonal to NMHC IIC (CST, #8189S), mouse monoclonal to Paxillin (BD Biosciences, #610619), mouse monoclonal to pRLC at Ser19 (CST, #3675S). All staining incubation steps were carried out in 1% BSA in PBS. Samples were again washed and incubated with fluorescently coupled secondary antibodies and affinity probes. Secondary Alexa Fluor 488-, Alexa Fluor 647- and Cy3-labeled anti-mouse or anti-rabbit antibodies were from Jackson Immunoresearch (West Grove, USA). F-Actin was labeled using Alexa Fluor 488- or Alexa Fluor 647-coupled phalloidin (ThermoFisher Scientific #A12379 and #A22287) and the nucleus was stained with DAPI (Carl Roth #6335.1). Samples were mounted in Mowiol containing 1% N-proply gallate.

Fluorescence imaging and live cell experiments: Images of immunolabeled samples on cross-patterned substrates were taken on an AxioimagerZ1 microscope (Carl Zeiss, Germany). To obtain high resolution images of bipolar minifilaments and heterotypic minifilaments, the AiryScan Modus of a confocal laser scanning microscope (LSM 800

AiryScan, Carl Zeiss) or a non-serial SR-SIM (Elyra PS.1, Carl Zeiss) were used. The grid for SR-SIM was rotated three times and shifted five times leading to 15 frames raw data of which a final SR-SIM image was calculated with the structured illumination package of ZEN software (Carl Zeiss, Germany). Channels were aligned by using a correction file that was generated by measuring channel misalignment of fluorescent tetraspecs (ThermoFischer, #T7280). All images were taken using a 63×, NA = 1.4 oil-immersion objective.
Live cell microscopy for flow measurements was carried out on a LSM 800 (Carl Zeiss, Germany), operating in the AiryScan mode with a 63× 1.4 NA oil-immersion objective. Prior to imaging, the incubation chamber was heated to 37°C. GFP-NM IIA transfected cells were seeded on FN-coated cell culture dishes (MatTek #P35G-1.5-14-C) or micropatterned substrates 3 h prior to imaging. During imaging, the cells were maintained in phenol red-free DMEM with HEPES and high glucose (ThermoFisher Scientific #21063029), supplemented with 10% bovine growth serum and 1% Pen/Strep. Images were taken every minute for up to 2 hours.

FRAP experiments and analysis: GFP-NM IIA or GFP-NM IIB transfected cells were seeded on FN-coated cell culture dishes (MatTek #P35G-1.5-14-C) 3 h prior to imaging. For Blebbistatin treated conditions, 50 µM photostable Para-Aminoblebbistatin (OptoPharma Ltd., Budapest, Hungary) was added to the medium 12 h prior to imaging.
FRAP experiments were performed on a LSM 800 (Carl Zeiss, Germany) equipped with a 63× 1.4 NA oil-immersion objective and operating in the confocal mode. Images were collected at pinhole 1.0 and maximum speed using the following conditions: 10 pre-bleach frames, photobleaching of the selected region using maximum laser power and 100 iterations, post-bleach acquisition with maximum speed (300 frames for GFP-NM IIA, GFP-NM IIA or GFP-NM IIB + Blebbistatin and 500 frames for GFP-NM IIB). At maximum speed, frame rates of 2-3 fps were reached.
To correct for drift, the feature detection and matching ORB-algorithm (Rublee et al., 2011) as implemented in openCV was applied to a temporal gaussian filtered image series. In slices of 20 frames features were detected and matched. Matches were used to determine a shift per frame. This shift per frame was used to align the original videos such that the regions of interest do not move. This was implemented in custom scripts. Two square regions of interest were defined in ImageJ: The bleach spot and a reference spot with similar pre-bleach intensity. In these regions the intensity was recorded as $I_{bleach}, I_{prebleach}, I_{ref}, I_{ref,prebleach}$the intensity of the bleached spot after bleaching, the mean intensity before bleaching, the intensity of the reference spot after bleaching and the mean intensity before bleaching respectively. The intensity was normalized and corrected for unwanted photobleaching with

$$I_{norm}(t) = \frac{I_{bleach}(t) - I_{bleach}(0)}{I_{prebleach}} \frac{I_{ref,prebleach}}{I_{ref}(t)}$$

The normalized intensities were fit to $I_{fit}(t) = \delta\big(1 - exp(-t/\tau)\big)$. The fit values were reported as recovery time $\tau$and mobile fraction δ.

Flow analysis, intensity and co-localization measurements: Flow in vSF or peripheral actin arcs was measured by creating kymographs from a ROI using the reslice function in ImageJ. From these kymographs, movement of individual, persistent minifilaments was tracked manually to determine the flow rate in nm/min.
Quantification of pRLC- and GFP-intensities were carried out by analyzing line scans along SF in the depicted region and calculating the mean intensity. For **Figure 4**, measurements were

taken from 30 cells out of three independent experiments with three line scans per cell. For the sake of clarity, data were normalized to the maximum value. In **Figure 4_figure supplement 1**, one plot shows absolute measurements from one representative experiment out of three independent. Each data point represents the mean value of one line scan from up to 12 analyzed cells with three line scans per cell.
Co-localization measurements in **figure 4_figure supplement 2** were carried out blinded by measuring the intensity of individual NMHC IIA-mApple clusters in the single channel mode, while the NM IIB-AF 488 channel was switched off. This way, preferential measurements of co-localizing NM IIA and NM IIB clusters were avoided. To calculate the ratio of NM IIA/NM IIB in different subcellular regions, intensities for both, NM IIA and NM IIB, were summed up and the percentage of each isoform was determined. Measurements were taken from three independent experiments with a total number of 32 polarized or not polarized cells. For each cell, mean values of line scans along minifilament clusters were taken in the depicted regions.

Quantification of FA parameters and *R*(*d*) ratios: Quantification of FAs was performed using the pixel classification functionality of the image analysis suite ilastik (Berg et al., 2019). First, ilastik was trained to mark the cell area. In a separate classification project ilastik was trained to discern between FA and non-FA. The segmentations were exported in the .npy file format for analysis in custom scripts. To determine the number of FAs connected component analysis was applied to the segmented FAs as implemented in openCV 3.4.1.
Quantifications of *R*(*d*) ratios were carried out by manually fitting circles to the peripheral actin arcs of cells on cross-patterned substrates. The spanning distance *d* was defined as the cell area covering the passivated substrate area. In cases, where the cell was polymerizing actin along the functionalized substrate without surpassing the complete distance to the cell edges (as observed in the case of NM IIA-KO cells), only the distance of the cell body covering the passive substrate was taken into account.

Modeling: FRAP trajectories of singular heterotypic minifilaments were simulated with a stochastic crossbridge and assembly model that is described in more detail in the supplemental text. We simulated for times equivalent to the experiments. The model returns trajectories of the number of fluorescent myosins in one heterotypic minifilament. Four independent trajectories were added up to obtain the FRAP intensity, which was normalized such that the initial intensity before bleaching was one. These intensity trajectories were analyzed in the same manner as the normalized experimental intensity trajectories.
For more information about the dTEM and the parameters, we also refer the reader to the supplemental text, where a detailed description can be found.

Acknowledgments

This work is supported by the Deutsche Forschungsgemeinschaft (DFG, German Research Foundation) under Germany's Excellence Strategy through EXC 2082/1-390761711 (the Karlsruhe-Heidelberg 3DMM2O Excellence Cluster, to USS and MB) and EXC 2181/1 - 390900948 (the Heidelberg STRUCTURES Excellence Cluster, to USS). USS is a member of the Interdisciplinary Center for Scientific Computing (IWR) at Heidelberg. JG acknowledges support by the Research Training Group of the Landesstiftung Baden-Württemberg on Mathematical Modeling for the Quantitative Biosciences.

Competing interests

We declare that no competing financial interests exist.

References

Anscombe, N. 2010. Direct laser writing. *Nature Photonics*. 4:22-23.

Balaban, N.Q., U.S. Schwarz, D. Riveline, P. Goichberg, G. Tzur, I. Sabanay, D. Mahalu, S. Safran, A. Bershadsky, L. Addadi, and B. Geiger. 2001. Force and focal adhesion assembly: a close relationship studied using elastic micropatterned substrates. *Nature cell biology*. 3:466-472.

Bar-Ziv, R., T. Tlusty, E. Moses, S.A. Safran, and A. Bershadsky. 1999. Pearling in cells: a clue to understanding cell shape. *Proceedings of the National Academy of Sciences of the United States of America*. 96:10140-10145.

Barua, B., A. Nagy, J.R. Sellers, and S.E. Hitchcock-DeGregori. 2014. Regulation of nonmuscle myosin II by tropomyosin. *Biochemistry*. 53:4015-4024.

Beach, J.R., K.S. Bruun, L. Shao, D. Li, Z. Swider, K. Remmert, Y. Zhang, M.A. Conti, R.S. Adelstein, N.M. Rusan, E. Betzig, and J.A. Hammer. 2017. Actin dynamics and competition for myosin monomer govern the sequential amplification of myosin filaments. *Nature cell biology*. 19:85-93.

Beach, J.R., L. Shao, K. Remmert, D. Li, E. Betzig, and J.A. Hammer, 3rd. 2014. Nonmuscle myosin II isoforms coassemble in living cells. *Current biology : CB*. 24:1160-1166.

Berg, S., D. Kutra, T. Kroeger, C.N. Straehle, B.X. Kausler, C. Haubold, M. Schiegg, J. Ales, T. Beier, M. Rudy, K. Eren, J.I. Cervantes, B. Xu, F. Beuttenmueller, A. Wolny, C. Zhang, U. Koethe, F.A. Hamprecht, and A. Kreshuk. 2019. ilastik: interactive machine learning for (bio)image analysis. *Nature methods*. 16:1226-1232.

Betapudi, V., L.S. Licate, and T.T. Egelhoff. 2006. Distinct roles of nonmuscle myosin II isoforms in the regulation of MDA-MB-231 breast cancer cell spreading and migration. *Cancer research*. 66:4725-4733.

Billington, N., A. Wang, J. Mao, R.S. Adelstein, and J.R. Sellers. 2013. Characterization of three full-length human nonmuscle myosin II paralogs. *The Journal of biological chemistry*. 288:33398-33410.

Bischofs, I.B., F. Klein, D. Lehnert, M. Bastmeyer, and U.S. Schwarz. 2008. Filamentous network mechanics and active contractility determine cell and tissue shape. *Biophysical journal*. 95:3488-3496.

Brand, C.A., M. Linke, K. Weissenbruch, B. Richter, M. Bastmeyer, and U.S. Schwarz. 2017. Tension and Elasticity Contribute to Fibroblast Cell Shape in Three Dimensions. *Biophysical journal*. 113:770-774.

Breckenridge, M.T., N.G. Dulyaninova, and T.T. Egelhoff. 2009. Multiple regulatory steps control mammalian nonmuscle myosin II assembly in live cells. *Molecular biology of the cell*. 20:338-347.

Bridgman, P.C., S. Dave, C.F. Asnes, A.N. Tullio, and R.S. Adelstein. 2001. Myosin IIB is required for growth cone motility. *The Journal of neuroscience : the official journal of the Society for Neuroscience*. 21:6159-6169.

Cai, Y., N. Biais, G. Giannone, M. Tanase, G. Jiang, J.M. Hofman, C.H. Wiggins, P. Silberzan, A. Buguin, B. Ladoux, and M.P. Sheetz. 2006. Nonmuscle myosin IIA-dependent force inhibits cell spreading and drives F-actin flow. *Biophysical journal*. 91:3907-3920.

Chen, T.J., C.C. Wu, M.J. Tang, J.S. Huang, and F.C. Su. 2010. Complexity of the tensegrity structure for dynamic energy and force distribution of cytoskeleton during cell spreading. *PloS one*. 5:e14392.

Conti, M.A., S. Even-Ram, C. Liu, K.M. Yamada, and R.S. Adelstein. 2004. Defects in cell adhesion and the visceral endoderm following ablation of nonmuscle myosin heavy chain II-A in mice. *The Journal of biological chemistry*. 279:41263-41266.

Dasbiswas, K., S. Hu, F. Schnorrer, S.A. Safran, and A.D. Bershadsky. 2018. Ordering of myosin II filaments driven by mechanical forces: experiments and theory. *Philosophical transactions of the Royal Society of London. Series B, Biological sciences*. 373.

del Rio, A., R. Perez-Jimenez, R. Liu, P. Roca-Cusachs, J.M. Fernandez, and M.P. Sheetz. 2009. Stretching single talin rod molecules activates vinculin binding. *Science*. 323:638-641.

Doyle, A.D., M.L. Kutys, M.A. Conti, K. Matsumoto, R.S. Adelstein, and K.M. Yamada. 2012. Micro-environmental control of cell migration--myosin IIA is required for efficient migration in fibrillar environments through control of cell adhesion dynamics. *Journal of cell science*. 125:2244-2256.

Dulyaninova, N.G., R.P. House, V. Betapudi, and A.R. Bresnick. 2007. Myosin-IIA heavy-chain phosphorylation regulates the motility of MDA-MB-231 carcinoma cells. *Molecular biology of the cell*. 18:3144-3155.

Dulyaninova, N.G., V.N. Malashkevich, S.C. Almo, and A.R. Bresnick. 2005. Regulation of myosin-IIA assembly and Mts1 binding by heavy chain phosphorylation. *Biochemistry*. 44:6867-6876.

Ebrahim, S., T. Fujita, B.A. Millis, E. Kozin, X. Ma, S. Kawamoto, M.A. Baird, M. Davidson, S. Yonemura, Y. Hisa, M.A. Conti, R.S. Adelstein, H. Sakaguchi, and B. Kachar. 2013. NMII forms a contractile transcellular sarcomeric network to regulate apical cell junctions and tissue geometry. *Current biology : CB*. 23:731-736.

Endlich, N., C.A. Otey, W. Kriz, and K. Endlich. 2007. Movement of stress fibers away from focal adhesions identifies focal adhesions as sites of stress fiber assembly in stationary cells. *Cell motility and the cytoskeleton*. 64:966-976.

Even-Ram, S., A.D. Doyle, M.A. Conti, K. Matsumoto, R.S. Adelstein, and K.M. Yamada. 2007. Myosin IIA regulates cell motility and actomyosin-microtubule crosstalk. *Nature cell biology*. 9:299-309.

Fasano, G., and A. Franceschini. 1986. A multidimensional version of the Kolmogorov-Smirnov test. *Monthly Notices of the Royal Astronomical Society*. 225:155-170.

Fritz, M., and M. Bastmeyer. 2013. Microcontact printing of substrate-bound protein patterns for cell and tissue culture. *Methods in molecular biology*. 1018:247-259.

Grewe, J., and U.S. Schwarz. 2020a. Mechanosensitive self-assembly of myosin II minifilaments. *Physical review. E*. 101:022402.

Grewe, J., and U.S. Schwarz. 2020b. Rheology of mixed motor ensembles. *arxiv online preprint*:arXiv:2007.05518.

Gumbiner, B.M. 1996. Cell adhesion: the molecular basis of tissue architecture and morphogenesis. *Cell*. 84:345-357.

Heissler, S.M., and D.J. Manstein. 2013. Nonmuscle myosin-2: mix and match. *Cellular and molecular life sciences : CMLS*. 70:1-21.

Hotulainen, P., and P. Lappalainen. 2006. Stress fibers are generated by two distinct actin assembly mechanisms in motile cells. *The Journal of cell biology*. 173:383-394.

Hu, S., K. Dasbiswas, Z. Guo, Y.H. Tee, V. Thiagarajan, P. Hersen, T.L. Chew, S.A. Safran, R. Zaidel-Bar, and A.D. Bershadsky. 2017. Long-range self-organization of cytoskeletal myosin II filament stacks. *Nature cell biology*. 19:133-141.

Ingber, D.E. 2003. Tensegrity I. Cell structure and hierarchical systems biology. *Journal of cell science*. 116:1157-1173.

Jana, S.S., S. Kawamoto, and R.S. Adelstein. 2006. A specific isoform of nonmuscle myosin II-C is required for cytokinesis in a tumor cell line. *The Journal of biological chemistry*. 281:24662-24670.

Jegou, A., M.F. Carlier, and G. Romet-Lemonne. 2013. Formin mDia1 senses and generates mechanical forces on actin filaments. *Nature communications*. 4:1883.

Jiu, Y., R. Kumari, A.M. Fenix, N. Schaible, X. Liu, M. Varjosalo, R. Krishnan, D.T. Burnette, and P. Lappalainen. 2019. Myosin-18B Promotes the Assembly of Myosin II Stacks for Maturation of Contractile Actomyosin Bundles. *Current biology : CB*. 29:81-92 e85.

Jiu, Y., J. Peranen, N. Schaible, F. Cheng, J.E. Eriksson, R. Krishnan, and P. Lappalainen. 2017. Vimentin intermediate filaments control actin stress fiber assembly through GEF-H1 and RhoA. *Journal of cell science*. 130:892-902.

Kassianidou, E., D. Probst, J. Jager, S. Lee, A.L. Roguet, U.S. Schwarz, and S. Kumar. 2019. Extracellular Matrix Geometry and Initial Adhesive Position Determine Stress Fiber Network Organization during Cell Spreading. *Cell reports*. 27:1897-1909 e1894.

Kaufmann, T.L., and U.S. Schwarz. 2020. Electrostatic and bending energies predict staggering and splaying in nonmuscle myosin II minifilaments. *PLoS computational biology*. 16:e1007801.

Kolega, J. 1998. Cytoplasmic dynamics of myosin IIA and IIB: spatial 'sorting' of isoforms in locomoting cells. *Journal of cell science*. 111 (Pt 15):2085-2095.

Kovacs, M., J. Toth, C. Hetenyi, A. Malnasi-Csizmadia, and J.R. Sellers. 2004. Mechanism of blebbistatin inhibition of myosin II. *The Journal of biological chemistry*. 279:35557-35563.

Kovacs, M., F. Wang, A. Hu, Y. Zhang, and J.R. Sellers. 2003. Functional divergence of human cytoplasmic myosin II: kinetic characterization of the non-muscle IIA isoform. *The Journal of biological chemistry*. 278:38132-38140.

Kumar, S., I.Z. Maxwell, A. Heisterkamp, T.R. Polte, T.P. Lele, M. Salanga, E. Mazur, and D.E. Ingber. 2006. Viscoelastic retraction of single living stress fibers and its impact on cell shape, cytoskeletal organization, and extracellular matrix mechanics. *Biophysical journal*. 90:3762-3773.

Labouesse, C., A.B. Verkhovsky, J.J. Meister, C. Gabella, and B. Vianay. 2015. Cell shape dynamics reveal balance of elasticity and contractility in peripheral arcs. *Biophysical journal*. 108:2437-2447.

Lee, S., E. Kassianidou, and S. Kumar. 2018. Actomyosin stress fiber subtypes have unique viscoelastic properties and roles in tension generation. *Molecular biology of the cell*. 29:1992-2004.

Lehnert, D., B. Wehrle-Haller, C. David, U. Weiland, C. Ballestrem, B.A. Imhof, and M. Bastmeyer. 2004. Cell behaviour on micropatterned substrata: limits of extracellular matrix geometry for spreading and adhesion. *Journal of cell science*. 117:41-52.

Lo, C.M., D.B. Buxton, G.C. Chua, M. Dembo, R.S. Adelstein, and Y.L. Wang. 2004. Nonmuscle myosin IIb is involved in the guidance of fibroblast migration. *Molecular biology of the cell*. 15:982-989.

Ma, X., S.S. Jana, M.A. Conti, S. Kawamoto, W.C. Claycomb, and R.S. Adelstein. 2010. Ablation of nonmuscle myosin II-B and II-C reveals a role for nonmuscle myosin II in cardiac myocyte karyokinesis. *Molecular biology of the cell*. 21:3952-3962.

Mandriota, N., C. Friedsam, J.A. Jones-Molina, K.V. Tatem, D.E. Ingber, and O. Sahin. 2019. Cellular nanoscale stiffness patterns governed by intracellular forces. *Nature materials*. 18:1071-1077.

Martinez, G.F., N.G. Gazal, G. Quassollo, A.M. Szalai, E.D. Cid-Pellitero, T.M. Durcan, E.A. Fon, M. Bisbal, F.D. Stefani, and N. Unsain. 2020. Quantitative expansion microscopy for the characterization of the spectrin periodic skeleton of axons using fluorescence microscopy. *Scientific reports*. 10:2917.

Matthews, B.D., D.R. Overby, R. Mannix, and D.E. Ingber. 2006. Cellular adaptation to mechanical stress: role of integrins, Rho, cytoskeletal tension and mechanosensitive ion channels. *Journal of cell science*. 119:508-518.

Mrksich, M., L.E. Dike, J. Tien, D.E. Ingber, and G.M. Whitesides. 1997. Using microcontact printing to pattern the attachment of mammalian cells to self-assembled monolayers of alkanethiolates on transparent films of gold and silver. *Experimental cell research*. 235:305-313.

Mrksich, M., and G.M. Whitesides. 1996. Using self-assembled monolayers to understand the interactions of man-made surfaces with proteins and cells. *Annual review of biophysics and biomolecular structure*. 25:55-78.

Oakes, P.W., E. Wagner, C.A. Brand, D. Probst, M. Linke, U.S. Schwarz, M. Glotzer, and M.L. Gardel. 2017. Optogenetic control of RhoA reveals zyxin-mediated elasticity of stress fibres. *Nature communications*. 8:15817.

Pato, M.D., J.R. Sellers, Y.A. Preston, E.V. Harvey, and R.S. Adelstein. 1996. Baculovirus expression of chicken nonmuscle heavy meromyosin II-B. Characterization of alternatively spliced isoforms. *The Journal of biological chemistry*. 271:2689-2695.

Peacock, J.A. 1983. Two-dimensional goodness-of-fit testing in astronomy. *Monthly Notices of the Royal Astronomical Society*. 202:615-627.

Qi, J., Y. Liu, C. Chu, X. Chen, W. Zhu, Y. Shu, S. He, R. Chai, and G. Zhong. 2019. A cytoskeleton structure revealed by super-resolution fluorescence imaging in inner ear hair cells. *Cell discovery*. 5:12.

Rai, V., D.G. Thomas, J.R. Beach, and T.T. Egelhoff. 2017. Myosin IIA Heavy Chain Phosphorylation Mediates Adhesion Maturation and Protrusion in Three Dimensions. *The Journal of biological chemistry*. 292:3099-3111.

Ran, F.A., P.D. Hsu, J. Wright, V. Agarwala, D.A. Scott, and F. Zhang. 2013. Genome engineering using the CRISPR-Cas9 system. *Nature protocols*. 8:2281-2308.

Rublee, E., V. Rabaud, K. Konolige, and G. Bradski. 2011. ORB: an efficient alternative to SIFT or SURF. *Proceedings / IEEE International Conference on Computer Vision*. Conference Paper.

Ruprecht, V., P. Monzo, A. Ravasio, Z. Yue, E. Makhija, P.O. Strale, N. Gauthier, G.V. Shivashankar, V. Studer, C. Albiges-Rizo, and V. Viasnoff. 2017. How cells respond to environmental cues - insights from bio-functionalized substrates. *Journal of cell science*. 130:51-61.

Russell, R.J., A.Y. Grubbs, S.P. Mangroo, S.E. Nakasone, R.B. Dickinson, and T.P. Lele. 2011. Sarcomere length fluctuations and flow in capillary endothelial cells. *Cytoskeleton*. 68:150-156.

Sandquist, J.C., and A.R. Means. 2008. The C-terminal tail region of nonmuscle myosin II directs isoform-specific distribution in migrating cells. *Molecular biology of the cell*. 19:5156-5167.

Sandquist, J.C., K.I. Swenson, K.A. Demali, K. Burridge, and A.R. Means. 2006. Rho kinase differentially regulates phosphorylation of nonmuscle myosin II isoforms A and B during cell rounding and migration. *The Journal of biological chemistry*. 281:35873-35883.

Scarpa, E., and R. Mayor. 2016. Collective cell migration in development. *The Journal of cell biology*. 212:143-155.

Schiller, H.B., M.R. Hermann, J. Polleux, T. Vignaud, S. Zanivan, C.C. Friedel, Z. Sun, A. Raducanu, K.E. Gottschalk, M. Thery, M. Mann, and R. Fassler. 2013. beta1- and alphav-class integrins cooperate to regulate myosin II during rigidity sensing of fibronectin-based microenvironments. *Nature cell biology*. 15:625-636.

Shelden, E.A., Z.T. Colburn, and J.C. Jones. 2016. Focusing super resolution on the cytoskeleton. *F1000Research*. 5.

Shellard, A., and R. Mayor. 2019. Supracellular migration - beyond collective cell migration. *Journal of cell science*. 132.

Shih, W., and S. Yamada. 2010. Myosin IIA dependent retrograde flow drives 3D cell migration. *Biophysical journal*. 98:L29-31.

Shutova, M., C. Yang, J.M. Vasiliev, and T. Svitkina. 2012. Functions of nonmuscle myosin II in assembly of the cellular contractile system. *PloS one*. 7:e40814.

Shutova, M.S., S.B. Asokan, S. Talwar, R.K. Assoian, J.E. Bear, and T.M. Svitkina. 2017. Self-sorting of nonmuscle myosins IIA and IIB polarizes the cytoskeleton and modulates cell motility. *The Journal of cell biology*. 216:2877-2889.

Shutova, M.S., W.A. Spessott, C.G. Giraudo, and T. Svitkina. 2014. Endogenous species of mammalian nonmuscle myosin IIA and IIB include activated monomers and heteropolymers. *Current biology : CB*. 24:1958-1968.

Sunyer, R., V. Conte, J. Escribano, A. Elosegui-Artola, A. Labernadie, L. Valon, D. Navajas, J.M. Garcia-Aznar, J.J. Munoz, P. Roca-Cusachs, and X. Trepat. 2016. Collective cell durotaxis emerges from long-range intercellular force transmission. *Science*. 353:1157-1161.

Svitkina, T. 2018. The Actin Cytoskeleton and Actin-Based Motility. *Cold Spring Harbor perspectives in biology*. 10.

Tabdanov, E.D., V.V. Puram, Z. Win, A. Alamgir, P.W. Alford, and P.P. Provenzano. 2018. Bimodal sensing of guidance cues in mechanically distinct microenvironments. *Nature communications*. 9:4891.

Takeda, K., H. Kishi, X. Ma, Z.X. Yu, and R.S. Adelstein. 2003. Ablation and mutation of nonmuscle myosin heavy chain II-B results in a defect in cardiac myocyte cytokinesis. *Circulation research*. 93:330-337.

Thery, M., A. Pepin, E. Dressaire, Y. Chen, and M. Bornens. 2006. Cell distribution of stress fibres in response to the geometry of the adhesive environment. *Cell motility and the cytoskeleton*. 63:341-355.

Thomas, D.G., A. Yenepalli, C.M. Denais, A. Rape, J.R. Beach, Y.L. Wang, W.P. Schiemann, H. Baskaran, J. Lammerding, and T.T. Egelhoff. 2015. Non-muscle myosin IIB is critical for nuclear translocation during 3D invasion. *The Journal of cell biology*. 210:583-594.

Thoresen, T., M. Lenz, and M.L. Gardel. 2013. Thick filament length and isoform composition determine self-organized contractile units in actomyosin bundles. *Biophysical journal*. 104:655-665.

Tojkander, S., G. Gateva, A. Husain, R. Krishnan, and P. Lappalainen. 2015. Generation of contractile actomyosin bundles depends on mechanosensitive actin filament assembly and disassembly. *eLife*. 4:e06126.

Tojkander, S., G. Gateva, G. Schevzov, P. Hotulainen, P. Naumanen, C. Martin, P.W. Gunning, and P. Lappalainen. 2011. A molecular pathway for myosin II recruitment to stress fibers. *Current biology : CB*. 21:539-550.

Trepat, X., and E. Sahai. 2018. Mesoscale physical principles of collective cell organization. *Nature Physics*. 14:671-682.

Tullio, A.N., D. Accili, V.J. Ferrans, Z.X. Yu, K. Takeda, A. Grinberg, H. Westphal, Y.A. Preston, and R.S. Adelstein. 1997. Nonmuscle myosin II-B is required for normal development of the mouse heart. *Proceedings of the National Academy of Sciences of the United States of America*. 94:12407-12412.

Tullio, A.N., P.C. Bridgman, N.J. Tresser, C.C. Chan, M.A. Conti, R.S. Adelstein, and Y. Hara. 2001. Structural abnormalities develop in the brain after ablation of the gene encoding nonmuscle myosin II-B heavy chain. *The Journal of comparative neurology*. 433:62-74.

Untergasser, A., I. Cutcutache, T. Koressaar, J. Ye, B.C. Faircloth, M. Remm, and S.G. Rozen. 2012. Primer3--new capabilities and interfaces. *Nucleic acids research*. 40:e115.

Uren, D., H.K. Hwang, Y. Hara, K. Takeda, S. Kawamoto, A.N. Tullio, Z.X. Yu, V.J. Ferrans, N. Tresser, A. Grinberg, Y.A. Preston, and R.S. Adelstein. 2000. Gene dosage affects the cardiac and brain phenotype in nonmuscle myosin II-B-depleted mice. *The Journal of clinical investigation*. 105:663-671.

Varkuti, B.H., M. Kepiro, I.A. Horvath, L. Vegner, S. Rati, A. Zsigmond, G. Hegyi, Z. Lenkei, M. Varga, and A. Malnasi-Csizmadia. 2016. A highly soluble, non-phototoxic, non-fluorescent blebbistatin derivative. *Scientific reports*. 6:26141.

Vicente-Manzanares, M., M.A. Koach, L. Whitmore, M.L. Lamers, and A.F. Horwitz. 2008. Segregation and activation of myosin IIB creates a rear in migrating cells. *The Journal of cell biology*. 183:543-554.

Vicente-Manzanares, M., X. Ma, R.S. Adelstein, and A.R. Horwitz. 2009. Non-muscle myosin II takes centre stage in cell adhesion and migration. *Nature reviews. Molecular cell biology*. 10:778-790.

Vicente-Manzanares, M., K. Newell-Litwa, A.I. Bachir, L.A. Whitmore, and A.R. Horwitz. 2011. Myosin IIA/IIB restrict adhesive and protrusive signaling to generate front-back polarity in migrating cells. *The Journal of cell biology*. 193:381-396.

Vicente-Manzanares, M., J. Zareno, L. Whitmore, C.K. Choi, and A.F. Horwitz. 2007. Regulation of protrusion, adhesion dynamics, and polarity by myosins IIA and IIB in migrating cells. *The Journal of cell biology*. 176:573-580.

Wang, F., E.V. Harvey, M.A. Conti, D. Wei, and J.R. Sellers. 2000. A conserved negatively charged amino acid modulates function in human nonmuscle myosin IIA. *Biochemistry*. 39:5555-5560.

Wang, F., M. Kovacs, A. Hu, J. Limouze, E.V. Harvey, and J.R. Sellers. 2003. Kinetic mechanism of non-muscle myosin IIB: functional adaptations for tension generation and maintenance. *The Journal of biological chemistry*. 278:27439-27448.

Wassie, A.T., Y. Zhao, and E.S. Boyden. 2019. Expansion microscopy: principles and uses in biological research. *Nature methods*. 16:33-41.

Wei, Q., and R.S. Adelstein. 2000. Conditional expression of a truncated fragment of nonmuscle myosin II-A alters cell shape but not cytokinesis in HeLa cells. *Molecular biology of the cell*. 11:3617-3627.

Zand, M.S., and G. Albrecht-Buehler. 1989. What structures, besides adhesions, prevent spread cells from rounding up? *Cell motility and the cytoskeleton*. 13:195-211.

Figures

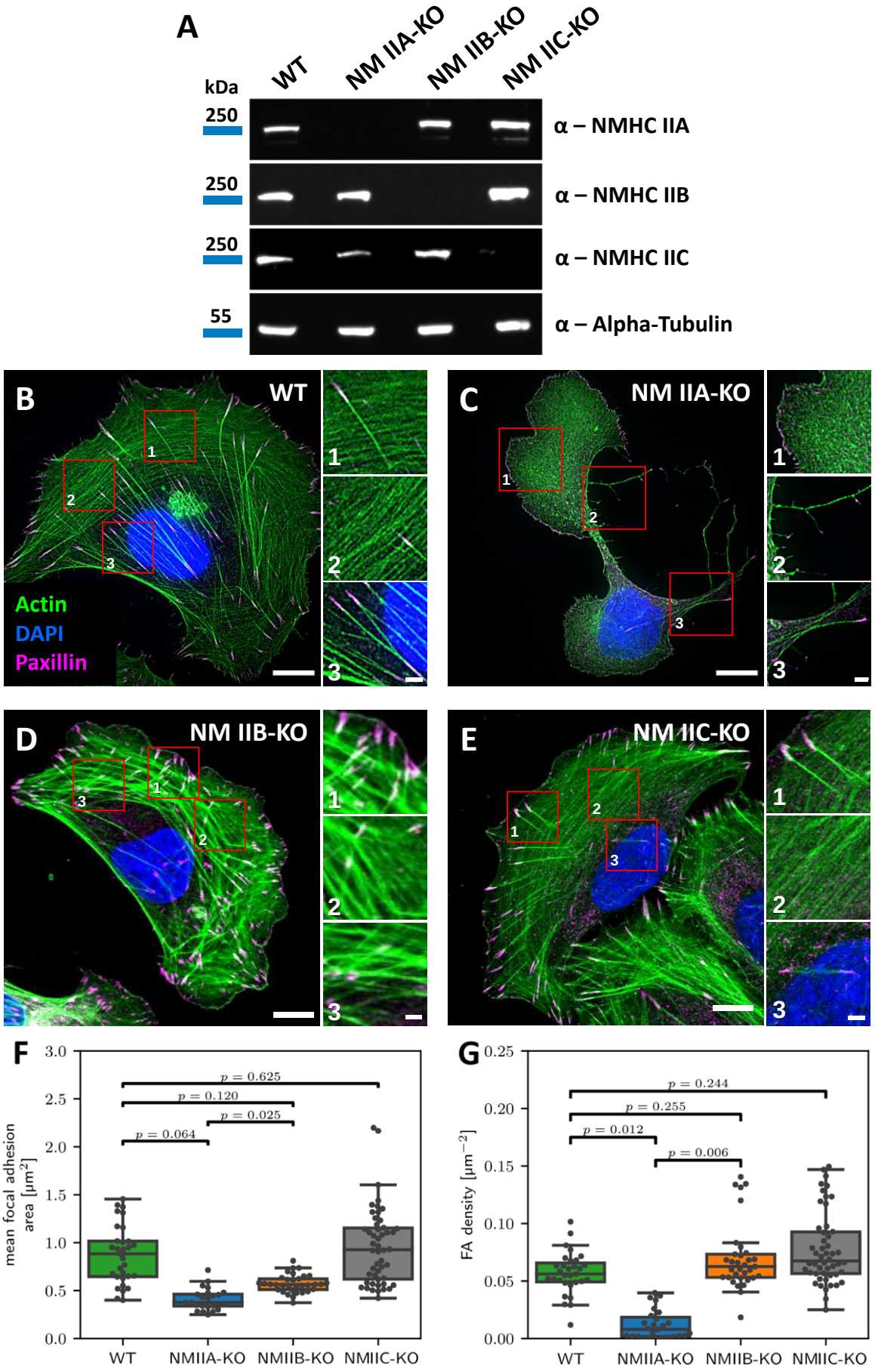
A
WT
NM IIA-KO
NM IIB-KO
NM IIC-KO
kDa
250
250
250
55
α – NMHC IIA
α – NMHC IIB
α – NMHC IIC
α – Alpha-Tubulin
B
WT
Actin
DAPI
Paxillin
C
NM IIA-KO
D
NM IIB-KO
E
NM IIC-KO
F
mean focal adhesion area [μm²]
p = 0.625
p = 0.120
p = 0.025
p = 0.064
WT
NMIIA-KO
NMIIB-KO
NMIIC-KO
G
FA density [μm⁻²]
p = 0.244
p = 0.255
p = 0.012
p = 0.006
WT
NMIIA-KO
NMIIB-KO
NMIIC-KO

Figure 1: Phenotypes of NM IIA, NM IIB, and NM IIC U2OS-KO cell lines are very distinct. **(A)** NM II-KO cell lines were generated via CRISPR/Cas9 and the loss of protein expression was confirmed via western blot. **(B)** U2OS WT cells show a polarized phenotype with prominent dorsal stress fibers (dSF) (1), transverse arcs (tA) (2), and ventral stress fibers (vSF) (3). Mature focal adhesions (FA) are visualized by elongated paxillin clusters that localize at the distal ends of dSF or both ends of vSF. **(C)** The NM IIA-KO leads to drastic morphological changes and the loss of most SFs and mature FAs. The overall actin structure resembles a dense meshwork of fine actin filaments (1). At the trailing edge, long cell extensions remain (2) and the only bundled actin fibers resemble vSF (3). **(D)** NM IIB-KO cells reveal slight changes in SF organization and FA structure. dSF (1), tA (2) and vSF (3) are present but their distinct localization pattern is disturbed. **(E)** The phenotype of NM IIC-KO cells is comparable to the WT. dSF (1), tA (2) and vSF (3) localize in a distinct pattern along the cell axis of polarized cells. **(F)** The mean FA area per cell is reduced for NM IIA-KO and NM IIB-KO cells, whereas FA density is only reduced in NM IIA-KO cells **(G)**. Quantifications are derived from three independent experiments (N = 3) and a total number of $n_{WT} = 31$; $n_{IIA\text{-}KO} = 27$; $n_{IIB\text{-}KO} = 33$ and $n_{IIC\text{-}KO} = 50$ cells. Scale bars represent 10 µm for overviews and 2 µm for insets of (B) - (E).

Figure 1_figure supplement 1: Knockout of NMHC IIA, NMHC IIB and NMHC IIC via CRISPR/Cas9.

Figure 1_figure supplement 2: FA number and cell area quantification.

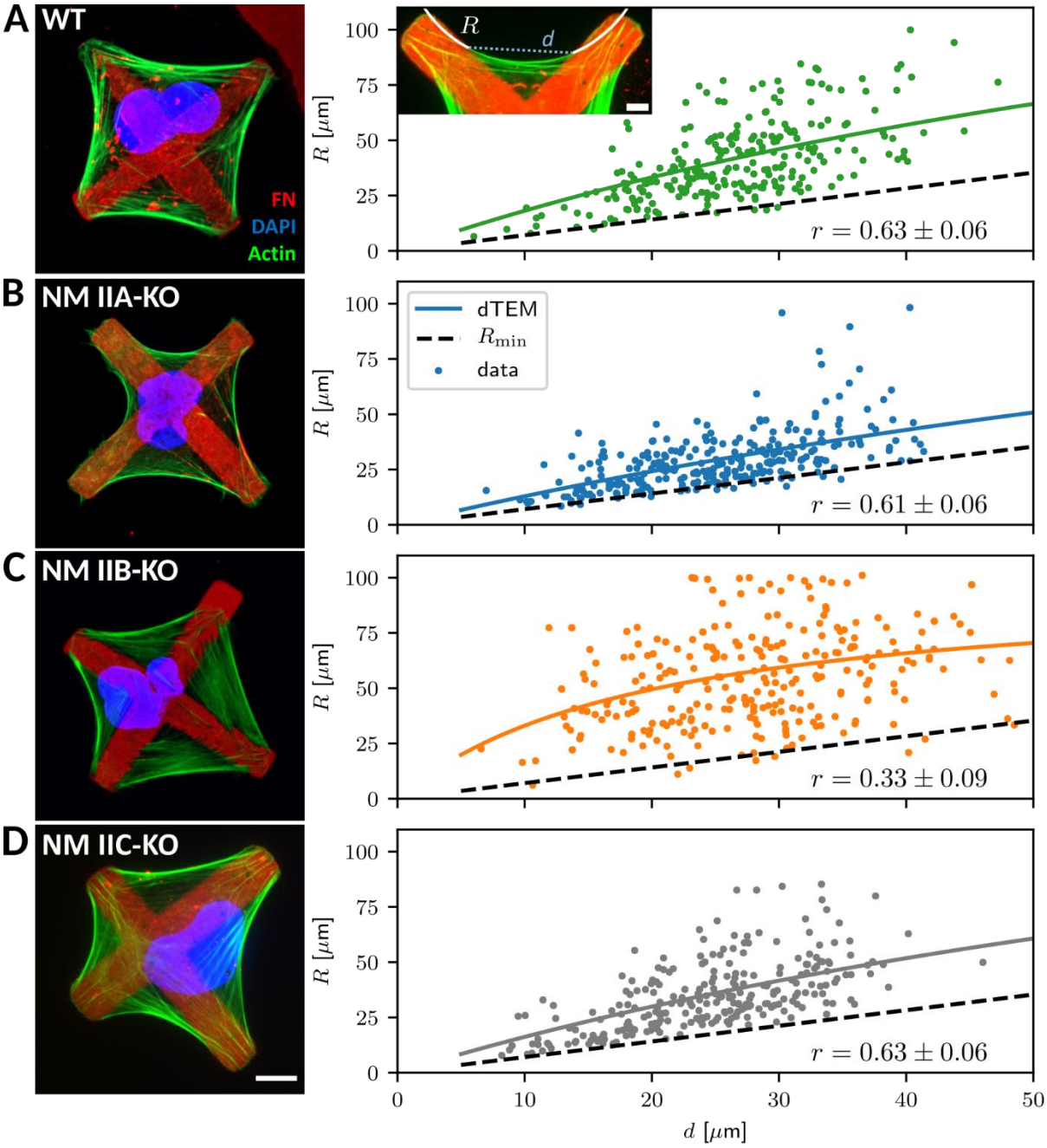

Figure 2: Quantitative shape analysis on cross-shaped micropatterns reveals distinct phenotypes for NM IIA-KO and NM IIB-KO cells.
(A) U2OS WT cells show prominent invaginated actin arcs along the cell contour, with an invagination radius *R* and a spanning distance *d* (see inset). Quantitative image analysis reveals a positive *R*(*d*) correlation (correlation coefficient r given at bottom right). Solid lines denote the bootstrapped mean fit of the dynamic tension-elasticity model (dTEM), black dashed lines denote the geometrically possible minimal radius. **(B)** U2OS NM IIA-KO cells form invaginated shapes on the cross-patterns despite their strongly perturbed shapes on homogeneous substrates. The spanning distance of the arcs is shorter, but the positive correlation between *R*(*d*) remains. **(C)** Actin arcs of U2OS NM IIB-KO cells are less invaginated compared to WT cells and the *R*(*d*)-correlation is very weak. **(D)** The phenotype of NM IIC-KO cells is comparable to WT and the *R*(*d*) correlation is not affected. Quantifications were derived from n_{WT} = 65; $n_{IIA\text{-}KO}$ = 83; $n_{IIB\text{-}KO}$ = 68 and $n_{IIC\text{-}KO}$ = 65 cells out of three independent experiments (N = 3). Scale bar represents 10 µm for (A) – (D).

Figure 2_figure supplement 1: Co-localization of NM IIA and NM IIB minifilaments along peripheral actin arcs.

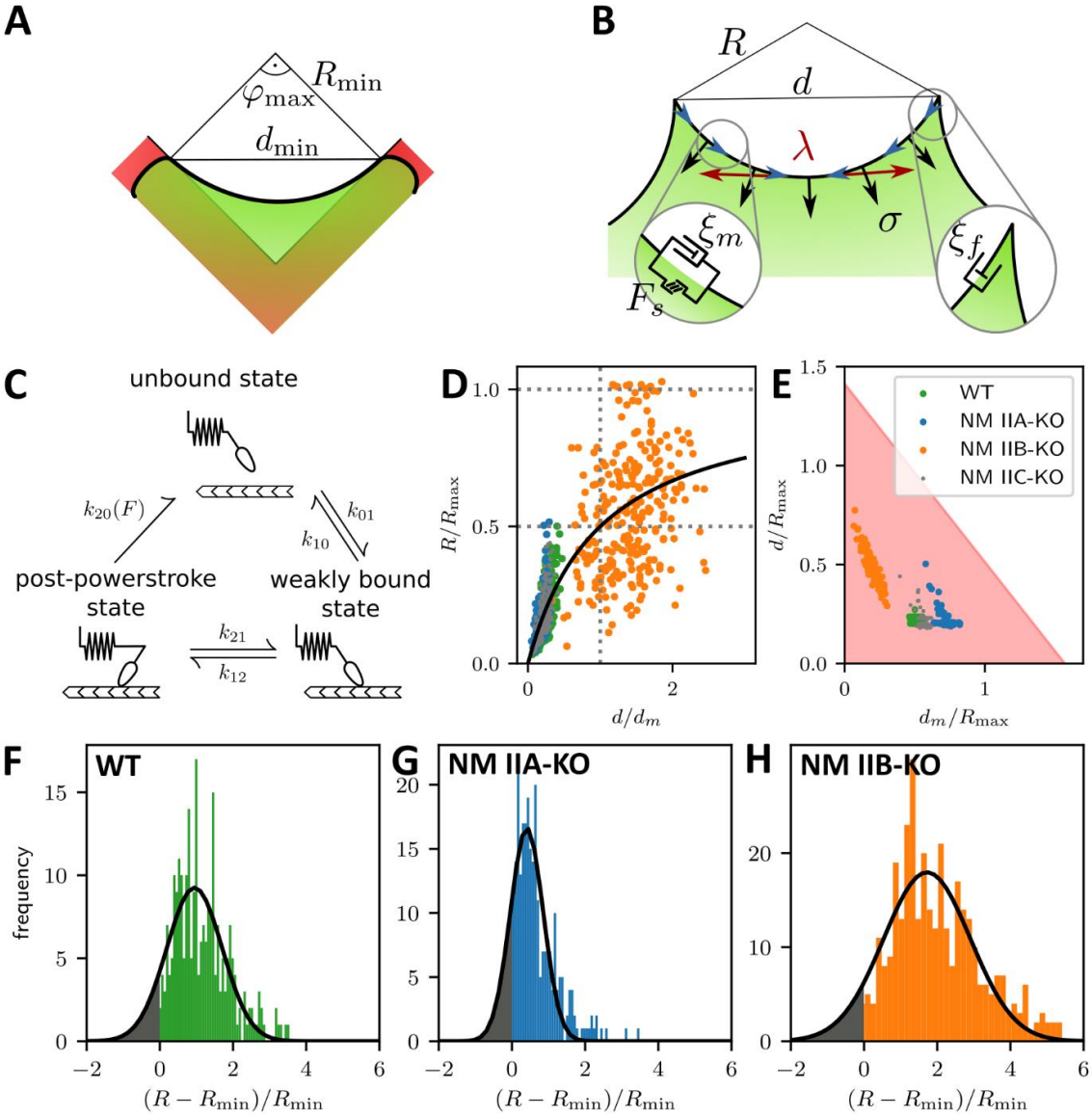

Figure 3: A dynamic tension-elasticity model (dTEM) connects the cellular phenotype to differences in the crossbridge cycling rates.

(A) Illustration depicting the geometrically possible minimal radius on the cross-shaped micropattern. The circular arcs on our cross pattern can have central angles of only up to 90°. **(B)** Schematics of the mathematical model. At each point along the cell contour, line tension λ and surface tension σ balance each other and thereby determine the circular arc shape. The insets show the frictional elements required to allow flow of the peripheral fiber (friction coefficients ξ_m and ξ_f for stress fibers and focal adhesions, respectively). The motor stall force is denoted as F_s. **(C)** Illustration depicting the three main mechanochemical states during the crossbridge cycle and the corresponding model rates. **(D)** Normalizing experimental results using the fit parameters from Figure 2 yields a master curve. WT, NM IIA-KO and NM IIC-KO cells fall into the linear regime, NM IIB-KO cells into the plateau regime, which corresponds to a loss of correlation. **(E)** d_m/R_{max} vs ratio of the maximum of the observed d-values to R_{max}. The region marked in red shows where the central angle of the arc is smaller than 90°. Points denote bootstrapped fit results. **(F-H)** Distributions of differences between observed radius and minimum allowed radius normalized to the minimally allowed radius resemble Gaussian distributions with cut-offs. From this we can estimate the fraction of non-formed rods (grey areas).

Figure 3_figure supplement 1: Cytoskeletal flow in SFs can be observed on homogenously coated substrates and cross-shaped micropattern.

Figure 3_movie 1: Cytoskeletal flow in SFs can be observed on homogenously coated substrates.

Figure 3_movie 2: Cytoskeletal flow in SFs can be observed on cross-shaped micropattern.

Figure 3_figure supplement 2: The dwell times of NM IIA and NM IIB in minifilaments influence the specific contractile output.

Figure 3_figure supplement 3: The dwell times of NM IIA and NM IIB in minifilaments influence the specific contractile output.

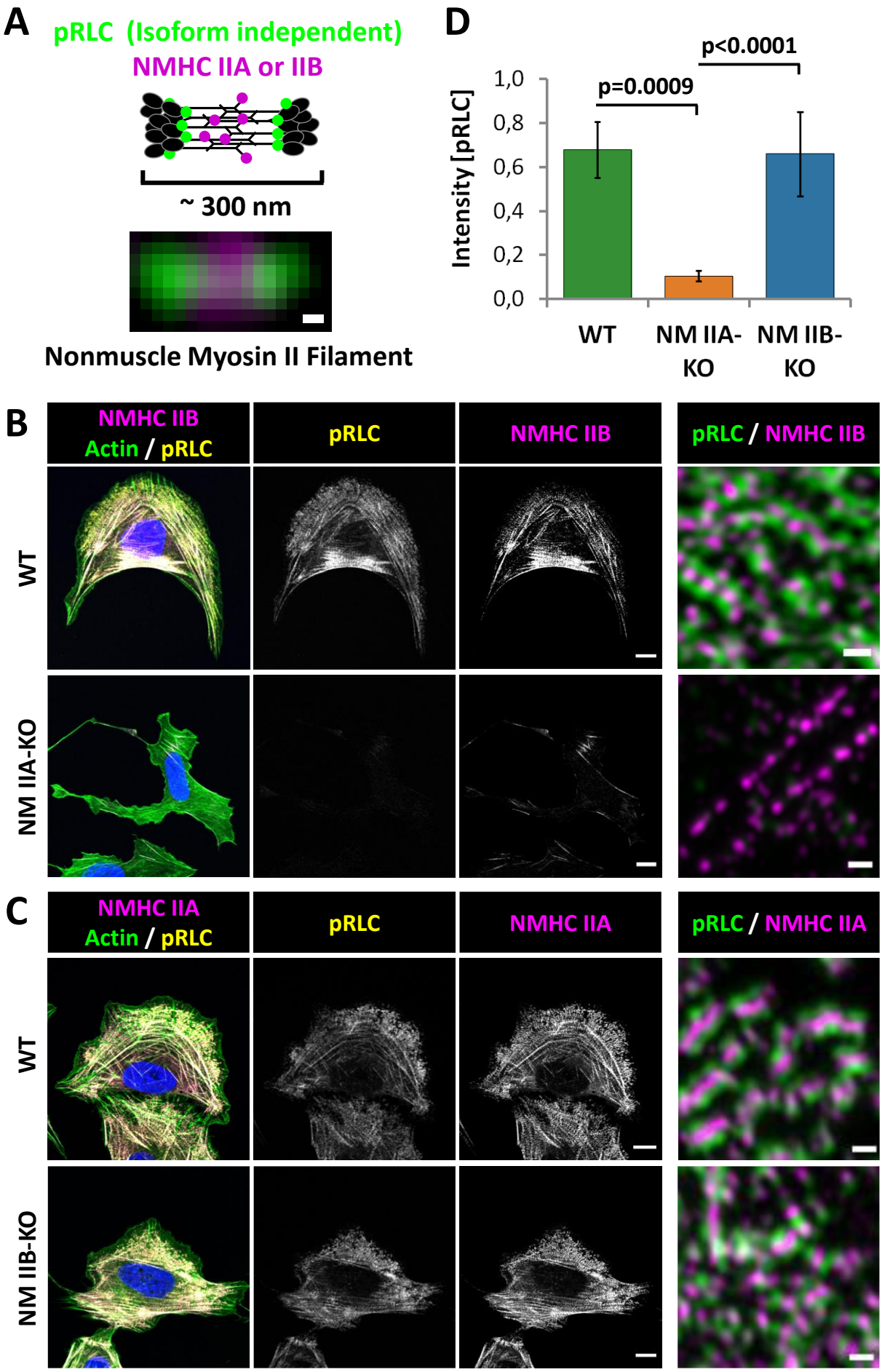
A
pRLC (Isoform independent)
NMHC IIA or IIB
~ 300 nm
Nonmuscle Myosin II Filament
D
p<0.0001
p=0.0009
Intensity [pRLC]
1,0
0,8
0,6
0,4
0,2
0,0
WT
NM IIA-KO
NM IIB-KO
B
NMHC IIB
Actin / pRLC
pRLC
NMHC IIB
pRLC / NMHC IIB
WT
NM IIA-KO
C
NMHC IIA
Actin / pRLC
pRLC
NMHC IIA
pRLC / NMHC IIA
WT
NM IIB-KO

1040

Figure 4: Loss of NM IIA prevents RLC phosphorylation and reduces NM IIB minifilament formation.
(A) Antibodies against the phosphorylated RLCs (pRLC) label the head regions of all active minifilaments (green), whereas isoform-specific antibodies label the tail regions of either NM IIA- or NM IIB-minifilaments (magenta) **(B)** In NM IIA-KO cells the signal of pRLC is almost completely absent and the number of NM IIB minifilaments is strongly reduced. **(C)** The loss of NM IIB does not affect the phosphorylation of the RLCs, nor the number and localization of NM IIA minifilaments. **(D)** pRLC signal intensity was quantified by measuring mean fluorescence intensity from line scans along SFs. Shown are normalized intensities from three independent experiments (N=3) and n=30 cells of each cell line. Scale bars represent 0.1 µm in (A), 10 µm in overviews and 0.5 µm in insets of (B) and (C).

Figure 4_figure supplement 1: RLC phosphorylation and NM IIB minifilament distribution correlates with the expression of NMHC IIA.

Figure 4_figure supplement 2: Formation of heterotypic NM IIA/NM IIB minifilaments is initiated by NM IIA.

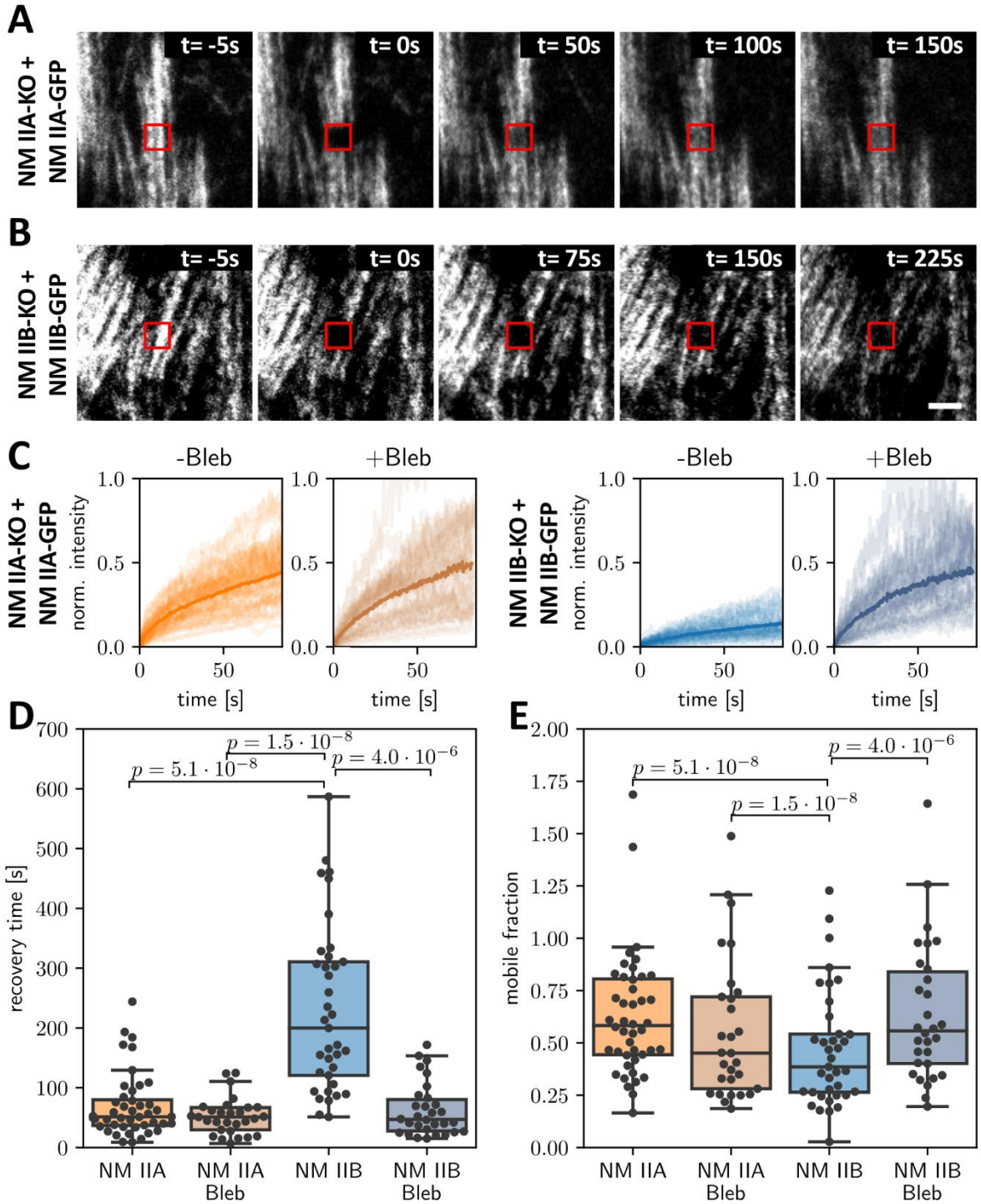

Figure 5: FRAP dynamics of NM IIA and NM IIB in the absence or presence of Blebbistatin are different.

(A) NM IIA or **(B)** NM IIB protein function was restored by expressing GFP-tagged NMHC IIA in NM IIA-KO or GFP-tagged NMHC IIB in NM IIB-KO cells, respectively. **(C)** Single recovery curves (thin lines) and average (thick line) for GFP-NMHC IIA or GFP-NMHC IIB in the absence or presence of photostable Para-Aminoblebbistatin (Bleb). **(D)** Boxplots showing the recovery time and **(E)** mobile fraction of GFP-NMHC IIA or GFP-NMHC IIB in the absence or presence of Para-Aminoblebbistatin. The recovery time of NM IIA is significantly faster compared to NM IIB and the mobile fraction is lower in the case of NM IIB. Treatment with Blebbistatin abolishes these differences, leading to similar recovery times and mobile fractions for both, NM IIA and NM IIB. Recovery times and mobile fractions were calculated from n_{IIA} = 45; $n_{IIA\text{-}Bleb}$ = 30; n_{IIB} = 37 and $n_{IIB\text{-}Bleb}$ = 30 individual traces and three independent experiments (N=3). For the sake of clarity, only p-values < 0.05 are shown. Scale bar represents 10 µm for (A) and (B).

Figure 5_movie 1: FRAP dynamics of NM IIA in the absence of Blebbistatin.

Figure 5_movie 2: FRAP dynamics of NM IIB in the absence of Blebbistatin.

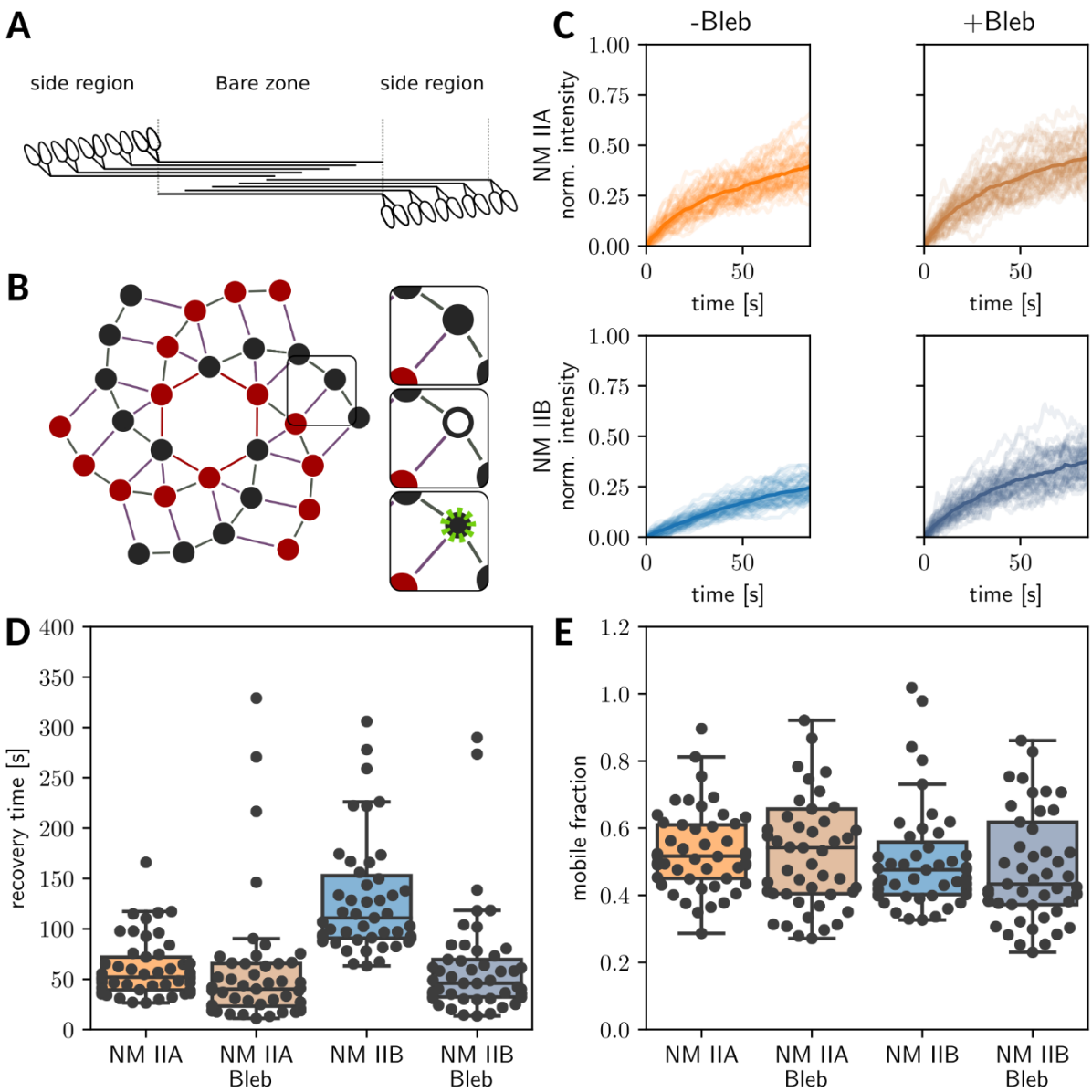

Figure 6: Stochastic computer simulations of the FRAP-experiments confirm the putative roles of the crossbridge cycling rates.

(A) 2D slice through the consensus architecture for myosin II minifilaments. **(B)** Graphical representation of the full 3D minifilament. Each node represents one myosin II hexamer. During FRAP, a bleached hexamer dissociates and a fluorescent hexamer enters. **(C)** Simulations of FRAP in the presence and absence of blebbistatin for mixed minifilaments with either NM IIA or NM IIB being fluorescent. Blebbistatin is assumed to decrease the crossbridge cycle rate k_{12} (compare Figure 3). **(D)** Recovery time and **(E)** mobile fraction predicted by the computer simulations.

Figure supplement

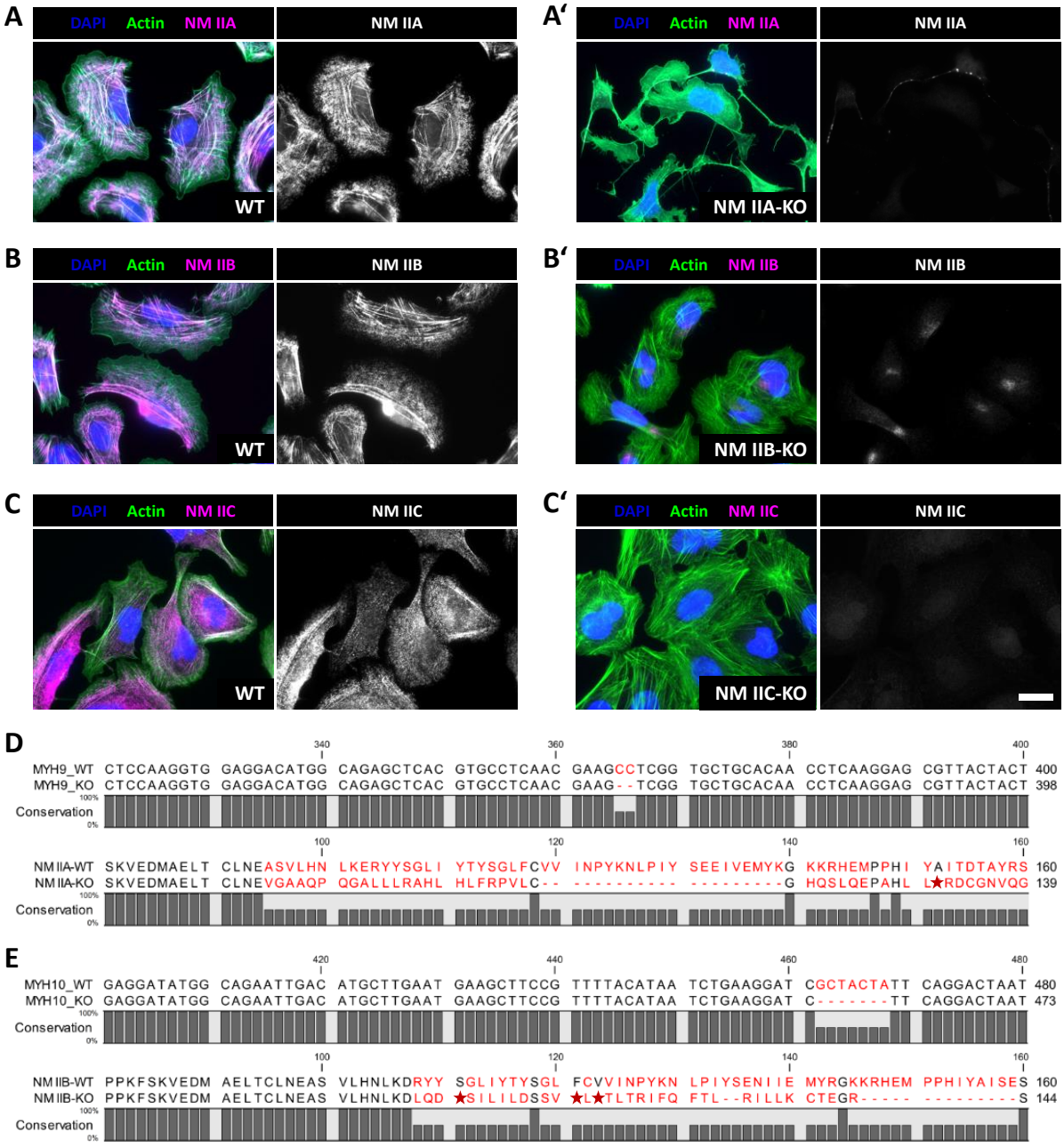

Figure 1_figure supplement 1: Knockout of NMHC IIA, NMHC IIB and NMHC IIC via CRISPR/Cas9. Immunofluorescent labeling was used to analyze the expression and localization of NM IIA **(A)**, NM IIB **(B)** and NM IIC **(C)** in U2OS WT cells. NM IIA and NM IIB showed a strict co-localization with actin fibers (labeled with phalloidin) throughout the cell body (NM IIA) or in the cell center (NM IIB) of polarized U2OS cells, while the NM IIC signals appeared more diffuse. Compared to WT cells, no signal for NMHC IIA **(A')**, NMHC IIB **(B')** or NMHC IIC **(C')** was detected in the corresponding KO cells. Deletions in the coding sequences of the first coding exons (exon 2) of NMHC IIA **(D)** and NMHC IIB **(E)** lead to frame shifts and premature stop codons in corresponding protein sequences (marked by asteriscs). Scale bars represent 20 µm for (A)-(C').

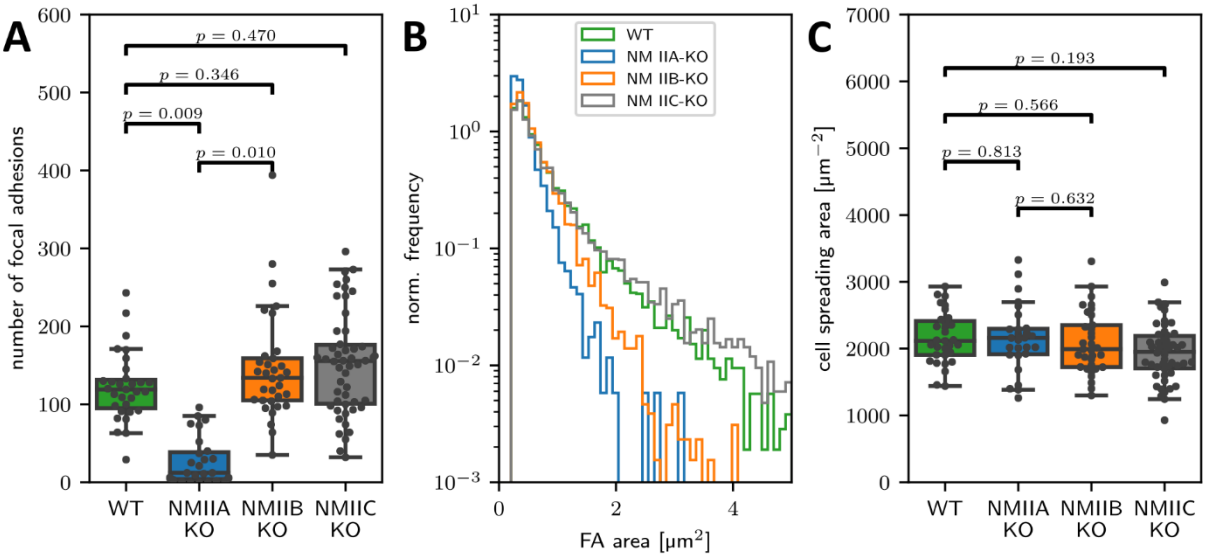

Figure 1_figure supplement 2: Quantification of FA number and cell spreading area. Quantifications showing the numbers of focal adhesion **(A)**, their size frequency **(B)**, and the cell area **(C)** of WT and the respective NM II-KO cell lines. **(A)** NM IIA-KO cells show a reduced number of mature focal adhesions (larger than 0.25 µm²), while no difference was observed for NM IIB-KO and NM IIC-KO cells. **(B)** The frequency distribution of FAs is shifted to smaller sizes in NM IIA-KO and NM IIB-KO cells as compared to WT cells. No difference was observed for NM IIC-KO cells. **(C)** The cell spreading area is not affected by the loss of NM IIA, NM IIB or NM IIC. Quantifications are derived from three independent experiments (N = 3) and a total number of $n_{WT} = 31$; $n_{IIA\text{-}KO} = 27$; $n_{IIB\text{-}KO} = 33$ and $n_{IIC\text{-}KO} = 50$ cells.

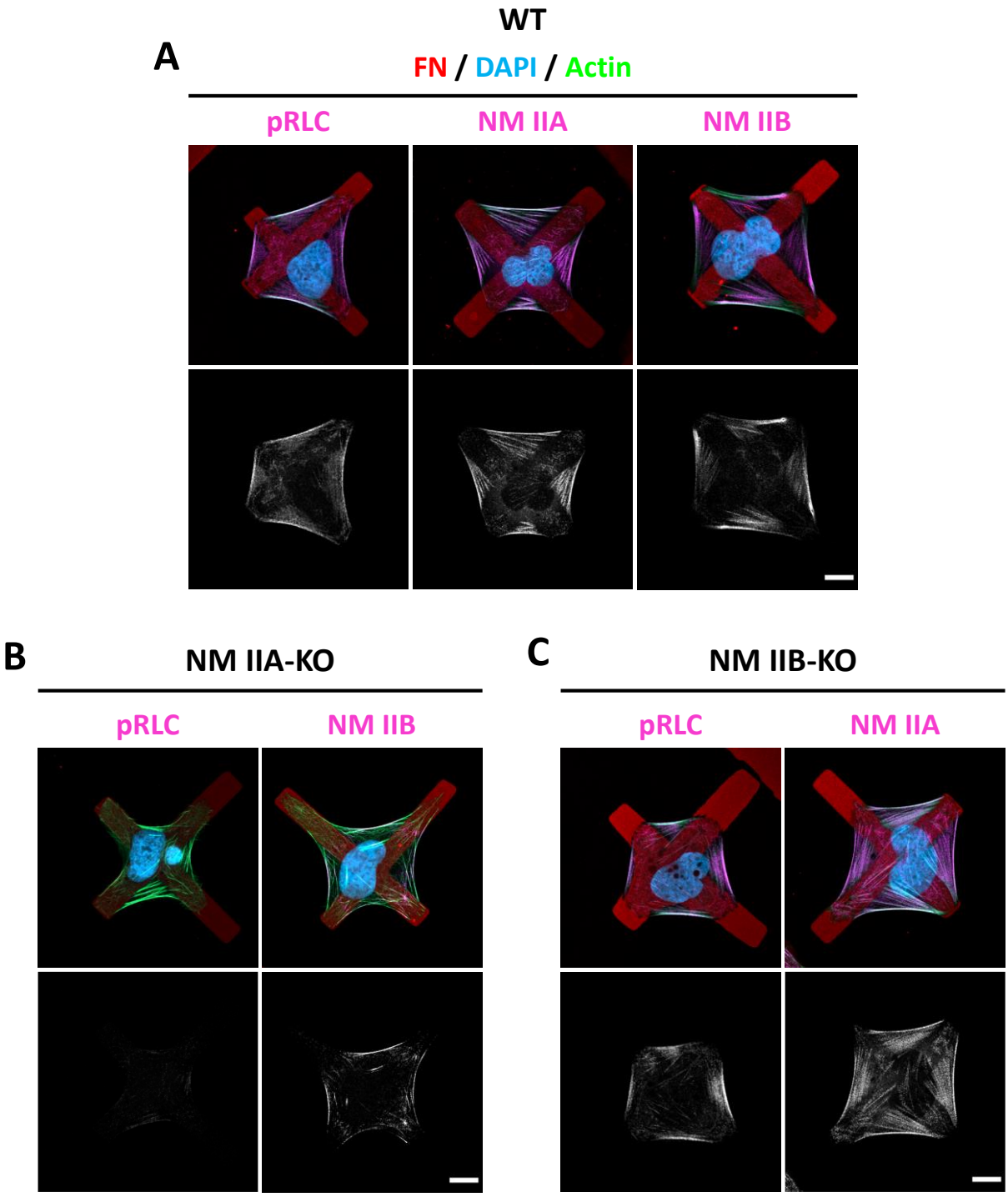

Figure 2_figure supplement 1: Localization of NM IIA and NM IIB minifilaments along peripheral actin arcs.
(A) In WT cells, NM IIA and NM IIB minifilaments localize along peripheral actin arcs and co-localize with pRLC staining. **(B)** In NM IIA-KO cells, fewer NM IIB minifilaments appear along the actin arcs and the pRLC staining is almost absent. **(C)** In NM IIB-KO cells, NM IIA minifilaments are still homogenously distributed along the actin arcs and the pRLC staining is comparable to WT cells. Scale bar represents 10 µm for A-C.

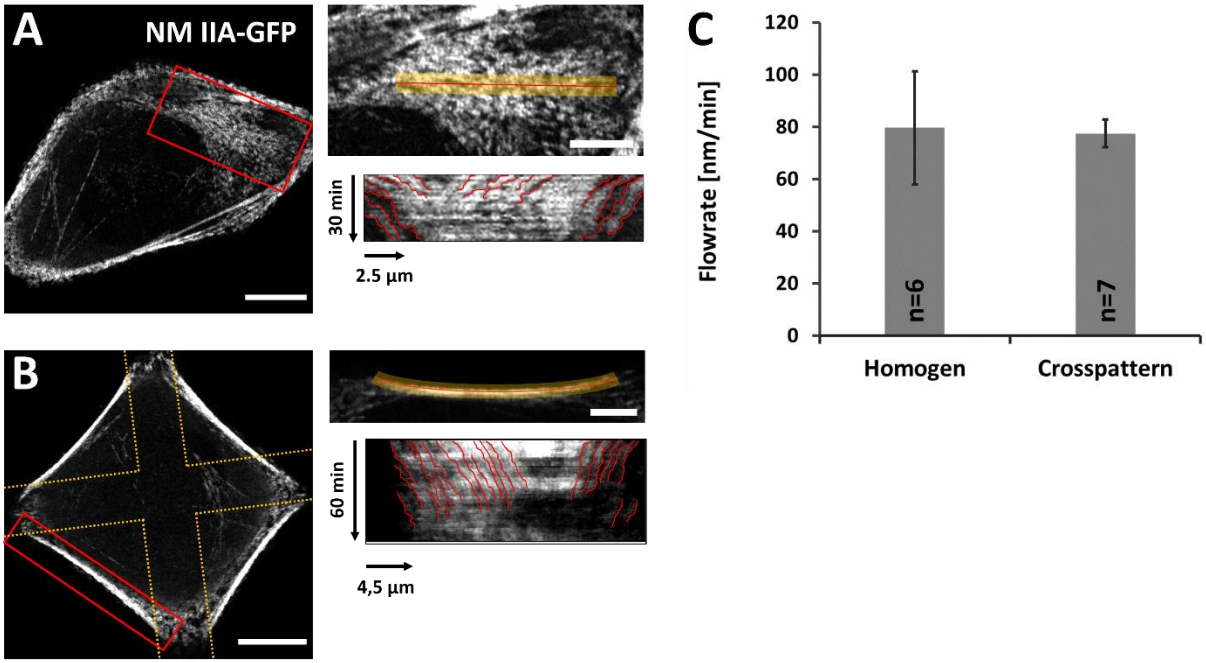

Figure 3_figure supplement 1: Cytoskeletal flow in actin SFs of cells on homogenously coated substrates and in actin arcs of cells on cross-shaped micropatterns.
U2OS WT cells were transfected with GFP-tagged NM IIA and cultivated on homogenously coated FN-substrates **(A)** or FN-coated cross-shaped micropatterns **(B)**. Images were taken every minute for up to 1h using the AiryScan Mode. Kymographs were derived using the reslice mode of FIJI. The cytoskeletal flow in the kymograph was tracked manually and the flowrate was calculated from individual traces (depicted in red). **(C)** Mean values and standard deviations from all traces (n=6 on homogeneously coated substrates and n=7 on cross-shaped micropattern). Scale bars represent 10 µm in overviews and 5 µm in insets of (A) and (B).

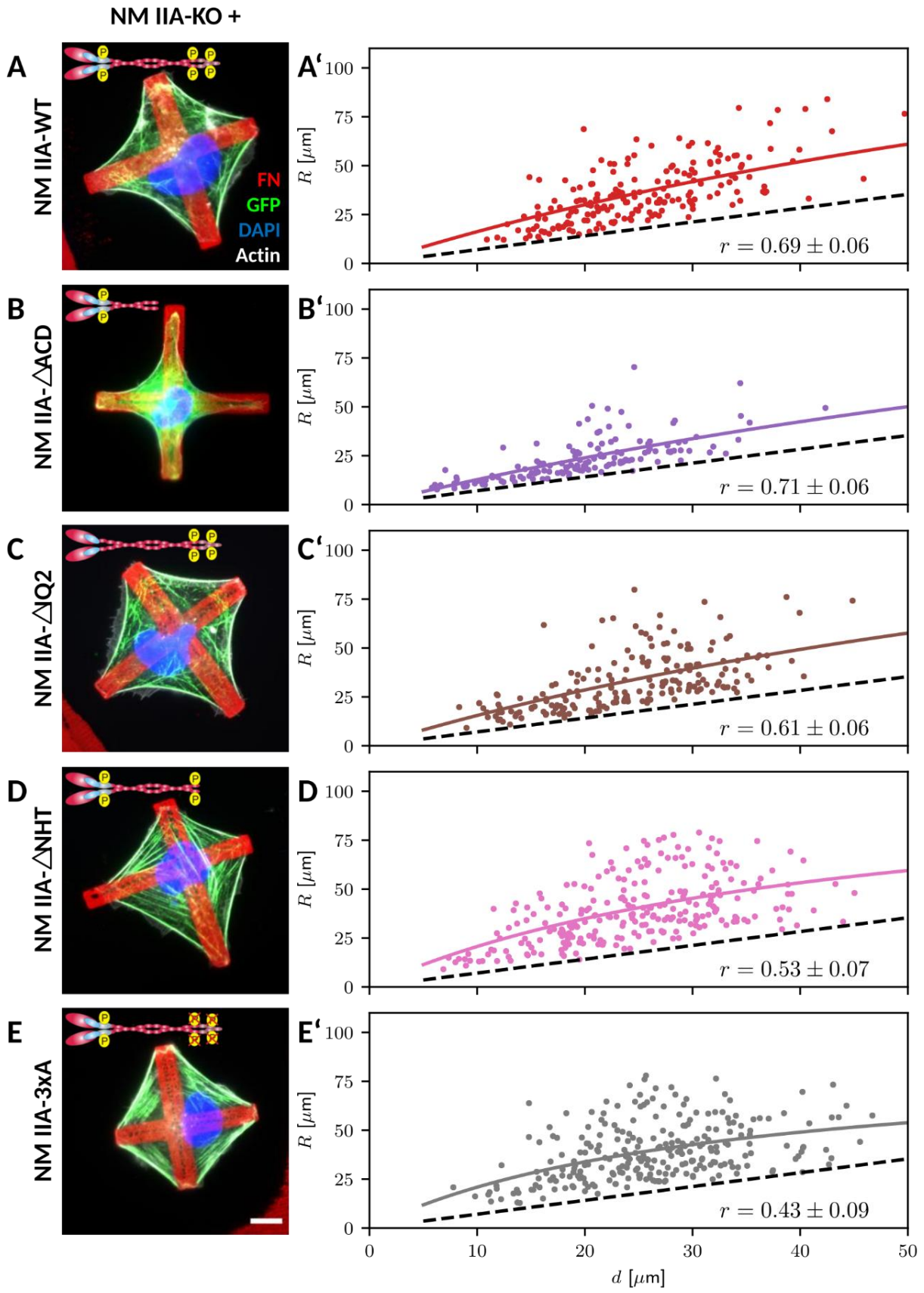

Figure 3_figure supplement 2: The dwell times of active NM IIA and NM IIB in minifilaments influence the specific contractile output.

NM IIA protein function was restored in NM IIA-KO cells by expressing different NMHC IIA constructs, which lead to a overassembly of NM IIA hexamers in minifilaments (Breckenridge et al., 2009; Dulyaninova et al., 2007; Dulyaninova et al., 2005; Rai et al., 2017). The cells were seeded on cross-

shaped micropatterns and the *R*(*d*) correlation was analyzed as described. **(A)** Restoring NM IIA-WT protein function does not affect the *R*(*d*) correlation. **(B)** Similarly, expressing NM IIA-ΔACD, which is unable to assemble into bipolar minifilaments, does not alter *R*(*d*) correlation. **(C)** Preventing RLC binding to the NMHC IIA by expressing NM IIA- ΔIQ2 leads to a constitutive active NM IIA molecule. Again this construct does not alter the *R*(*d*) correlation. **(D)** and **(E)**: Decreasing NM IIA disassembly rates by preventing c-terminal NMHC IIA phosphorylation (Dulyaninova et al., 2007; Dulyaninova et al., 2005) leads to a reduced *R*(*d*) correlation. This effect was observed when preventing phosphorylation at S1943 by expressing NM IIA-ΔNHT **(D)** and is even stronger when preventing phosphorylation on both prominent p-sites, S1943 and S1916, by expressing NM IIA-3xA **(E)**. Quantifications were derived from three independent experiments (N=3) with n_{WT} = 54; $n_{\Delta ACD}$ = 39; $n_{\Delta IQ2}$ = 50; $n_{\Delta NHT}$ = 70 and n_{3xA} = 72 cells. Scale bar represents 10 µm in (A)-(E).

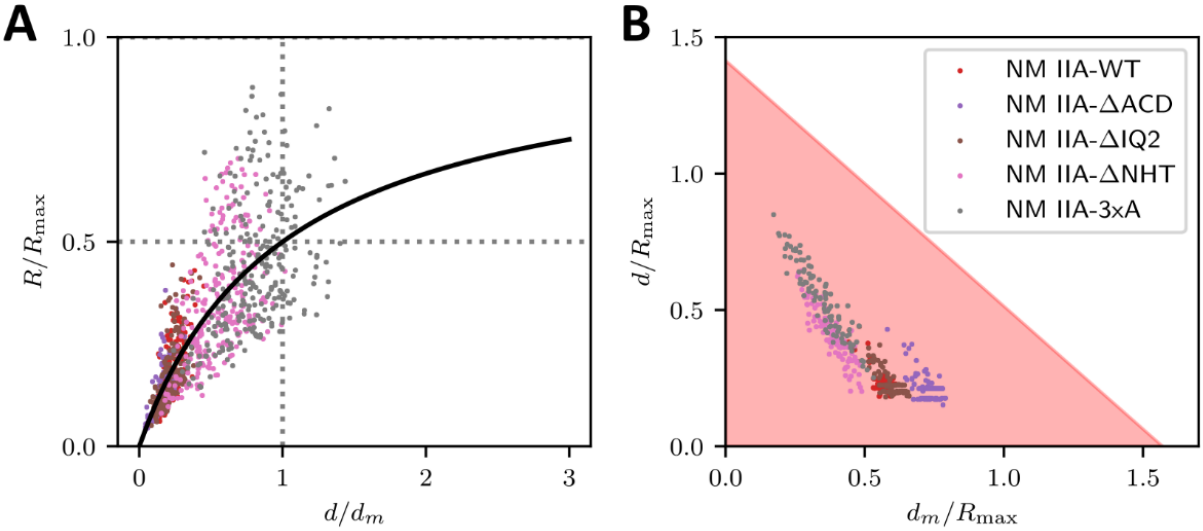

Figure 3_figure supplement 3: The dwell times of active NM IIA and NM IIB in minifilaments influence the specific contractile output.

Rescaling the experimental values from Figure 4_figure supplement 2 using the fit parameters shows that the contractile output depends on the dwell time of NM IIA and/or NM IIB in the minifilaments. **(A)** The longer the dwell time of NM IIA, the more the data points lie in the plateau regime of the dTEM master curve. Therefore, the data points from NM IIA-ΔNHT and NM IIA-3xA lie closest to the plateau regime, while NM IIA-WT, NM IIA-ΔACD and NM IIA-ΔIQ2 lie in the linear regime. **(B)** The ratio d_m/R_{max}, which scales linearly with the ratio of SF friction and motor stall force, shows the same distribution: NM IIA-ΔACD lies closest to the minimal possible radius, NM IIA-ΔNHT and NM IIA-3xA most far away.

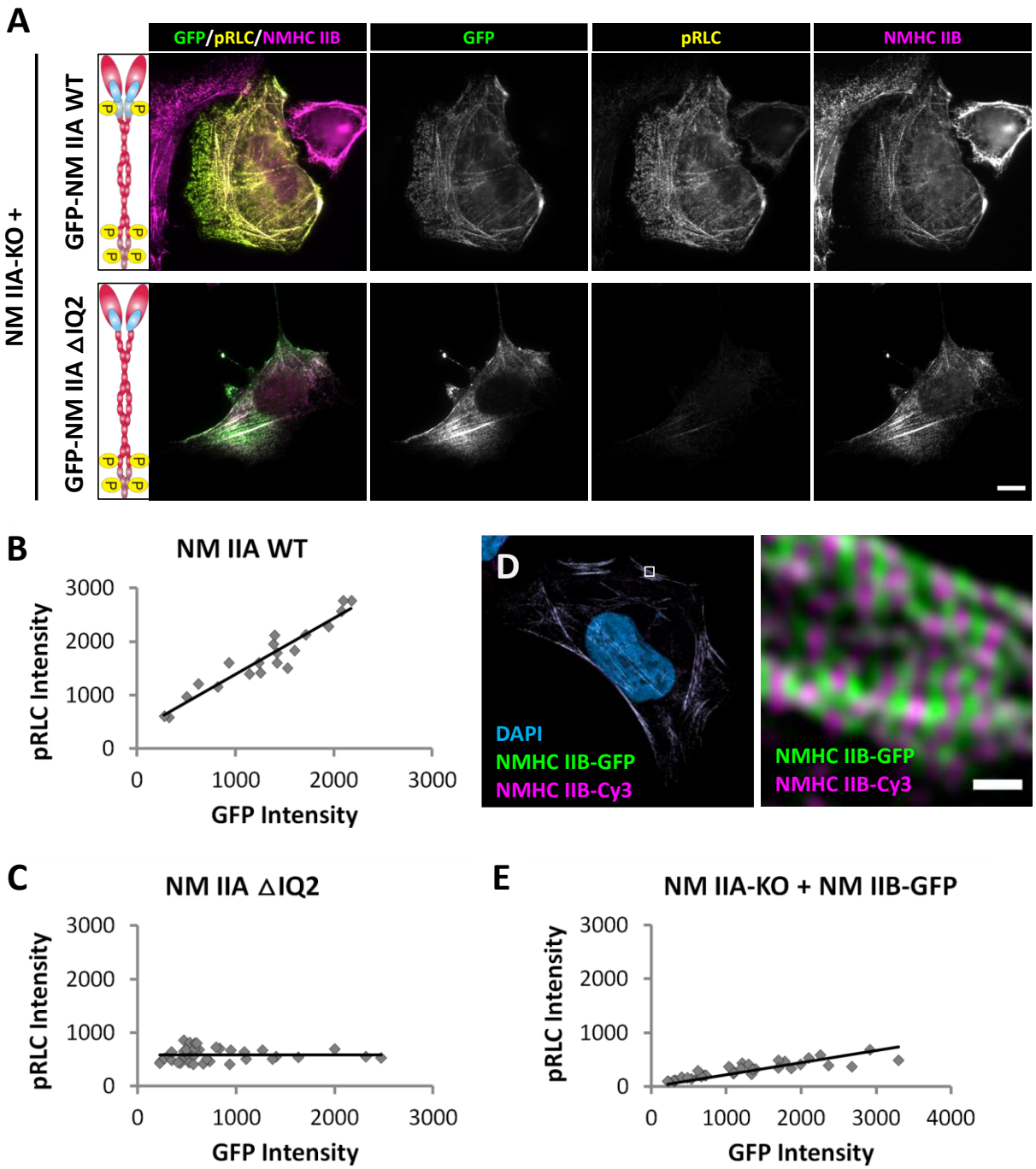

Figure 4_figure supplement 1: RLC phosphorylation and NM IIB minifilament distribution correlates with the expression of NM IIA.

The phosphorylation of the RLC and the localization of NM IIB is strongly affected by the expression of NM IIA. **(A)** and **(B)** Reconstitution of NM IIA in NM IIA-KO cells leads to a linear increase of pRLC signal with increasing GFP-NM IIA expression and restores NM IIB minifilaments. **(A)** and **(C)** Expression of NM IIA-ΔIQ2, which lacks the binding site for the RLC does not restore RLC phosphorylation but restores NM IIB minifilaments. **(D)** In NM IIA-KO cells, NM IIB minifilaments still possess a bipolar structure on their own, as visualized by the overexpression of N-terminal tagged NM IIB. **(E)** In this case, however, only a very modest increase in RLC phosphorylation was observed. Plots were derived from the following data sets: n_{WT} = 20 line scans from 7 cells; $n_{\Delta IQ2}$ = 39 line scans from 13 cells; $n_{IIB\text{-}GFP}$ = 36 line scans from 12 cells. The experiment was repeated three times (N=3). Scale bars represent 10 µm in (A) and (D) and 0.5 µm in the inset of (D).

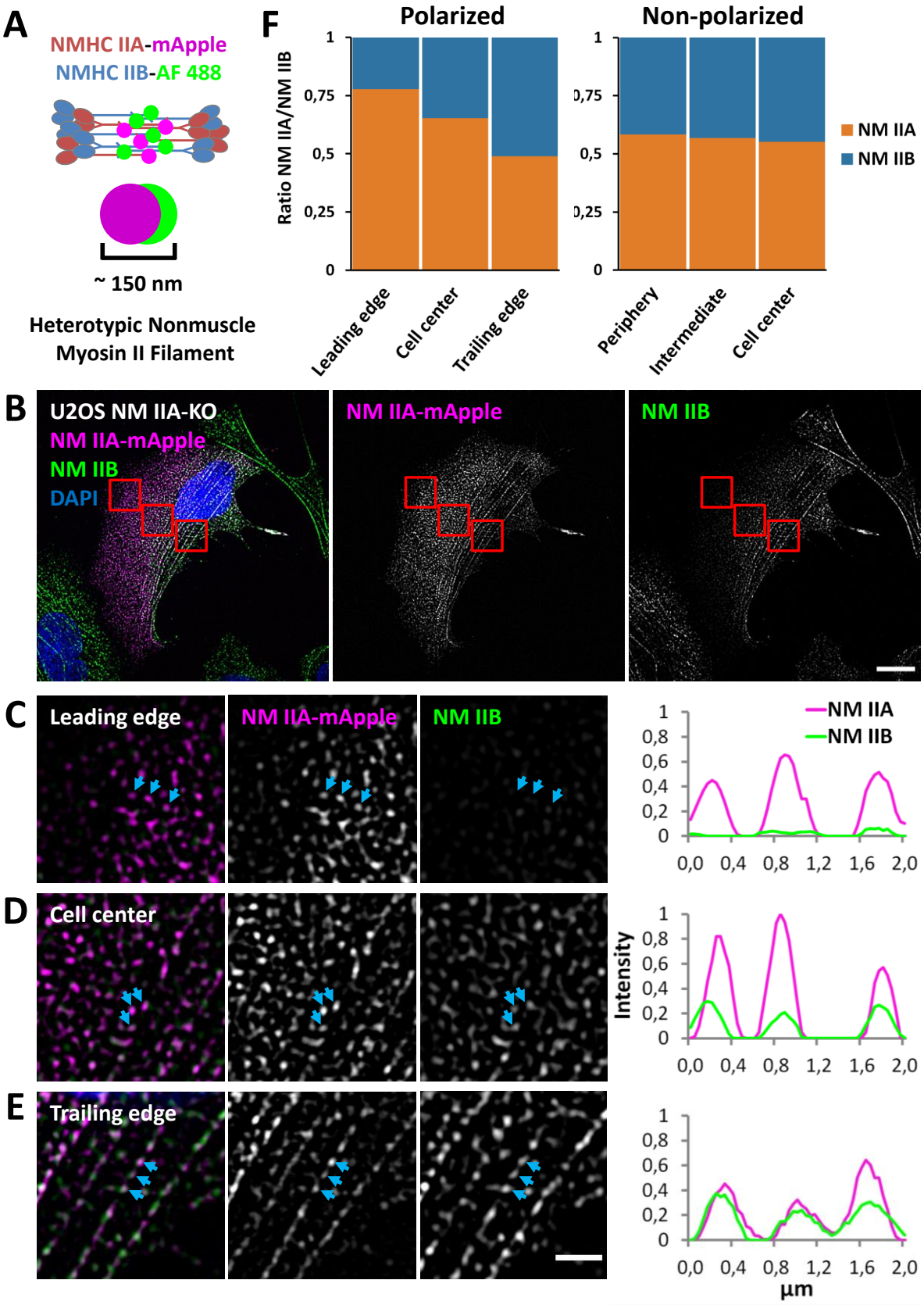

Figure 4_figure supplement 2: Formation of heterotypic NM IIA/NM IIB minifilaments is initiated by NM IIA.

(A) NM IIA-KO cells were reconstituted with c-terminal tagged NM IIA-mApple (magenta) and endogenous NM IIB was labeled by an antibody recognizing the c-terminal tailpiece of NM IIB (green). Co-localization of NM IIA and NM IIB clusters was analyzed along the cell axis of polarized or non-

polarized cells. **(B)** Example of a polarized cell with representative measurements in three different spots (red squares corresponding to (C)-(E)). **(C)** In polarized cells, homotypic NM IIA clusters were observed along the leading edge. Here, at the border to the lamellum, new minifilaments assemble and are translocated with the retrograde actin flow rearward to the cell center (Beach et al., 2017). Co-localization with NM IIB clusters was very low in these newly formed NM IIA minifilaments. **(D)** With increasing distance from the leading edge, NM IIB co-assembles into NM IIA minifilaments. **(E)** In the cell center, a balanced ratio of NM IIA and NM IIB in heterotypic minifilaments is achieved. Individual line scans depict co-localization of NM IIA and NM IIB in the three clusters, corresponding to the blue arrows. **(F)** While the ratio of NM IIA and NM IIB changed with regard to the centripetal actin flow in polarized cells, it remained constant in non-polarized cells. Line scans along SFs were derived from 16 individual polarized or non-polarized cells (n=32) out of three independent experiments (N=3). Scale bars represent 10 µm for overview in (B) and 2 µm in insets (C-E).

Tables

Table 1: Mean bootstrapped fit values for the invaginated arcs

Cell line	R_{max} [µm]	d_m [µm	d_m /R_{max}
WT	199 ± 5	100 ± 5	0.50 ± 0.02
NM IIA-KO	190 ± 24	137 ± 22	0.72 ± 0.04
NM IIB-KO	98 ± 18	20 ± 9	0.19 ± 0.05
NM IIC-KO	194 ± 19	110 ± 14	0.56 ± 0.03
NM IIA-KO + NM IIA-WT	195 ± 16	110 ± 12	0.56 ± 0.03
NM IIA-KO + NM IIA-ΔACD	184 ± 31	134 ± 26	0.72 ± 0.04
NM IIA-KO + NM IIA-ΔIQ2	180 ± 31	106 ± 23	0.58 ± 0.04
NM IIA-KO + NM IIA-ΔNHT	112 ± 28	44 ± 17	0.38 ± 0.06
NM IIA-KO + NM IIA-3xA	89 ± 24	33 ± 17	0.35 ± 0.08

The error is given as the standard deviation of the bootstrapped fit results. Note that the fit was bounded such that R_{max} < 200 µm. Therefore in cases where R_{max} is close to 200 µm the fit only gives reasonable error estimates for the quotient d_m /R_{max}.

Table 2: Primer and gRNA sequences

Description	Sequence
Myh9 gRNA sequence	5‘ GCACGTGCCTCAACGAAGCCT 3‘
Myh9 gRNA sequence (rc)	5‘ AGGCTTCGTTGAGGCACGTGC 3‘
Myh10 gRNA sequence	5‘ GCTGAAGGATCGCTACTATTC 3‘
Myh10 gRNA sequence (rc)	5‘ GAATAGTAGCGATCCTTCAGC 3‘
Myh14 gRNA sequence	5‘ GCGGAGTAGTACCGCTCCCGG 3‘
Myh14 gRNA sequence (rc)	5‘ CCGGGAGCGGTACTACTCCGC 3‘
*Myh9*_exon2 sense primer	5‘ GCAAAGAGAAGAGGTGTGAGC 3‘
*Myh9*_exon2 antisense primer	5‘ AGTTCAAGGATGTCACCCCA 3‘
*Myh10*_exon2 sense primer	5‘ GTTAGTATGGCTGTGAAGAGGT 3‘
*Myh10*_exon2 antisense primer	5‘ TCAAAGAAAAGCAAGACATGGGT 3‘